Iron from coal combustion particles dissolves much faster than mineral dust under simulated atmospheric acid conditions

Clarissa Baldo[1], Akinori Ito[2], Michael D. Krom[3,4], Weijun Li[5], Tim Jones[6], Nick Drake[7], Konstantin Ignatyev[8], Nicholas Davidson[1], Zongbo Shi[1]

[1]School of Geography Earth and Environmental Sciences, University of Birmingham, Birmingham, United Kingdom

[2]Yokohama Institute for Earth Sciences, JAMSTEC, Yokohama, Kanagawa 236-0001, Japan

[3]Morris Kahn Marine Station, Charney School of Marine Sciences, University of Haifa, Haifa, Israel

[4]School of Earth and Environment, University of Leeds, Leeds, United Kingdom

[5]Department of Atmospheric Sciences, School of Earth Sciences, Zhejiang University, Hangzhou 310027, China

[6]School of Earth and Environmental Sciences, Cardiff University, Cardiff, United Kingdom

[7]Department of Geography, King's College London, London, United Kingdom

[8]Diamond Light Source, Didcot, Oxfordshire, United Kingdom

Correspondence to: Zongbo Shi (z.shi@bham.ac.uk); Akinori Ito (akinori@jamstec.go.jp)

Abstract. Mineral dust is the largest source of aerosol iron (Fe) to the offshore global ocean, but acidic processing of coal fly ash (CFA) in the atmosphere could ~~be~~ be an important source of soluble aerosol Fe~~may result in a disproportionally higher contribution of bioavailable Fe~~. Here, we determined the Fe speciation and dissolution kinetics of CFA from Aberthaw (United Kingdom), Krakow (Poland), and Shandong (China) in solutions which simulate atmospheric acidic processing. In CFA-PM_{10} fractions, 8%-21.5% of the total Fe was as hematite and goethite (dithionite extracted Fe), 2%-6.5 % as amorphous Fe (ascorbate extracted Fe), while magnetite (oxalate extracted Fe) varied from 3%-22%. The remaining 50%-87 % of Fe was associated with other Fe-bearing phases, possibly aluminosilicates. High concentrations of ammonium ~~sulphate~~ sulfate ($(NH_4)_2SO_4$), often found in wet aerosols, increased Fe solubility of CFA up to 7 times at low pH (2-3). The oxalate effect on the Fe dissolution rates at pH 2 varied considerably depending on the samples, from no impact for Shandong ash to doubled dissolution for Krakow ash~~Our results showed a large variability in the effects of oxalate on the Fe dissolution rates at pH 2, from no impact in Shandong ash to doubled dissolution in Krakow ash~~. However, this enhancement was suppressed in the presence of high concentrations of $(NH_4)_2SO_4$. Dissolution of highly reactive (amorphous) Fe was insufficient to explain the high Fe solubility at low pH in CFA, and the modelled dissolution kinetics suggest~~s~~ that other Fe-bearing phases such as magnetite may also dissolve relatively rapidly under acidic conditions. Overall, Fe in CFA dissolved up to 7 times faster than in a Saharan dust precursor sample~~than in Saharan dust samples~~ at pH 2. Based on these laboratory data, we developed a new scheme for the proton- and oxalate- promoted Fe dissolution of CFA, which was implemented into the global atmospheric chemical transport model IMPACT. The revised model showed a better agreement with observations ~~of surface concentration~~ of ~~dissolved Fe~~Fe solubility in aerosol particles over the Bay of Bengal, due to the initial rapid release of Fe and the suppression of the oxalate-promoted dissolution at low pH~~due to the rapid Fe release at the initial stage at highly acidic conditions~~. The improved model ~~also~~ enabled us to predict sensitivity to a more dynamic range of pH changes, particularly between anthropogenic combustion and biomass burning aerosols.

1 Introduction

The availability of iron (Fe) limits primary productivity in high-nutrient low-chlorophyll (HNLC) regions of the global ocean including the subarctic North Pacific, the East Equatorial Pacific and the Southern Ocean (Boyd et al., 2007; Martin, 1990). In other regions of the global ocean such as the subtropical North Atlantic, the Fe input may affect primary productivity by stimulating nitrogen fixation (Mills et al., 2004; Moore et al., 2006). These areas are particularly sensitive to changes in the supply of bioavailable Fe. Atmospheric aerosols are an important source of soluble (and, thus potentially bio-accessible~~bioavailable~~) Fe to the offshore global ocean. The deposition of bio-accessible ~~bioavailable~~ Fe to the ocean can alter biogeochemical cycles and increase the carbon uptake, consequently affecting the climate (e.g., Jickells and Moore, 2015; Jickells et al., 2005; Kanakidou et al., 2018; Mahowald et al., 2010; Shi et al., 2012). In general, ~~bioavailable~~ bio-accessible Fe consists of aerosol dissolved Fe, and Fe-nanoparticles which can be present in the original particulate matter and/or formed during atmospheric transport as a result of cycling into and out of clouds (Shi et al., 2009). It is in addition possible that other more refractory forms of Fe could be solubilised in the surface waters by zooplankton (Schlosser et al., 2018) or the microbial community (Rubin et al., 2011).

The Fe transported in the atmosphere ~~Atmospheric Fe~~ is largely derived from lithogenic sources, which contribute around 95% of the total Fe in suspended particles (e.g.,Shelley et al., 2018) and ~~hence~~ most studies so far have concentrated on atmospheric processing of mineral dust (e.g., Cwiertny et al., 2008; Fu et al., 2010; Ito and Shi, 2016; Shi et al., 2011a; Shi et al., 2015). Mineral dust has low Fe solubility (dissolved Fe/ total Fe) near the source regions, generally below ~~0.5~~1% (e.g., Shi et al., 2011c; Sholkovitz et al., 2009; Sholkovitz et al., 2012), increasing somewhat as a result of processes occurring during atmospheric transport~~atmospheric processing~~ (e.g., Baker et al., 2021; Baker et al., 2020). Other sources of bio-accessible ~~bioavailable~~ Fe to the ocean are from combustion sources such as biomass burning, coal combustion, ~~and~~ oil combustion, and metal smelting ~~(e.g., shipping emissions)~~ (e.g., Ito et al., 2018; Rathod et al., 2020). Although these sources are only a small fraction of the total Fe in atmospheric particulates, the Fe solubility of pyrogenic sources can be 1–2 orders of magnitude higher than in mineral dust (Ito et al., 2021b and references therein), and thus can be important in promoting carbon uptake. However the Fe solubility of ~~these~~ pyrogenic sources ~~vary~~ varies considerably depending on the particular sources with higher values observed for oil combustion and biomass burning than coal combustion sources (Ito et al., 2021b and references therein).

Wang et al. (2015) estimated that coal combustion ~~produces~~ emitted around ~0.9 Tg yr^{-1} of ~~atmospheric~~ Fe into the atmosphere (on average for 1960–2007), contributing up to ~86% of the total anthropogenic Fe emissions. A more recent study, which has included metal smelting as an atmospheric Fe source, estimated that coal combustion emitted ~0.7 Tg yr^{-1} of Fe for the year 2010, contributing around 34% of the total anthropogenic Fe atmospheric loading (Rathod et al., 2020). Although the use of coal as a ~~principle~~ principal energy source has been recently reduced as a result of concern about air quality and global warming, coal is still an important energy source in a number of countries in particular in the Asia-Pacific region (BP, 2020). In China, most of the total energy is supplied by coal, contributing over 50% of the global coal consumption in 2019, followed by India (12%), and the US (8%). Germany and Poland are the largest coal consumers in Europe, accounting together for around 40% of the European usage (BP, 2020). South Africa is also among the principal countries for coal consumption (BP, 2020) and is a source of Fe-bearing particles to the ~~Fe-limited~~anaemic Southern Ocean (e.g., Ito et al., 2019).

Coal fly ash (CFA) is a by-product of coal combustion. This generally consists of glassy spherical particles (e.g., Brown et al., 2011), which are formed through different transformations (decomposition, fusion, agglomeration, volatilization) of mineral matter in coal during combustion (e.g., Jones, 1995), and are transported with the flue gases undergoing rapid solidification. CFA are co-emitted with acidic gases such as sul~~ph~~ur dioxide (SO_2), nitrogen oxides (NO_x) and carbon dioxide (CO_2) (e.g., Munawer, 2018).

During long-range transport, CFA particles undergo atmospheric processing with the CFA surface coated by acidic species such as ~~sulphuric~~ sulfuric acid (H_2SO_4) and oxalic acid ($H_2C_2O_4$) in atmospheric aerosols. Aged CFA particles are hygroscopic and absorb water at typical relative humidity in the marine atmosphere. As a result, ~~. This forms~~ a thin layer of water with high acidity, low pH and high ionic strength is formed around the particles (Meskhidze et al., 2003; Spokes and Jickells, 1995; Zhu et al., 1992). In addition, ammonia (NH_3) which is a highly hydrophilic gas, can also partition into the aerosol phase, react with H_2SO_4 and form ammonium ~~sulphate~~ sulfate ($(NH_4)_2SO_4$) an important inorganic salt contributing to the high ionic strength in ~~such~~ aged atmospheric aerosols (Seinfeld and Pandis, 2016).

~~-~~At low pH conditions, Fe solubility in aerosols increases, as the high concentration of protons (H^+) weakens the Fe-O bonds facilitating the detachment of Fe from the surface lattice (Furrer and Stumm, 1986). Li et al. (2017) provided the first observational evidence ~~to confirm~~ that ~~the~~ acidification leads to the release of Fe from anthropogenic particles.

In addition to these inorganic processes, organic ligands can also enhance atmospheric Fe dissolution by forming soluble complexes with Fe (e.g., Cornell and Schwertmann, 2003). For example, $H_2C_2O_4$ is an important organic species in ~~atmospheric~~ aerosols (e.g., Kawamura and Bikkina, 2016). Laboratory studies have demonstrated that $H_2C_2O_4$ increases Fe solubility of ~~atmospheric~~ aerosol sources (Chen and Grassian, 2013; Johnson and Meskhidze, 2013; Paris and Desboeufs, 2013; Paris et al., 2011; Xu and Gao, 2008). Recently, observations over the Bay of Bengal indicate that $H_2C_2O_4$ contributes to the increase of dissolved Fe in atmospheric water ~~dissolved Fe~~ (Bikkina et al., 2020).

To simulate the Fe dissolution in CFA, it is necessary to determine the dissolution kinetics under realistic conditions. Previous studies have investigated the Fe dissolution kinetics of CFA under acidic conditions. Chen et al. (2012) simulated acidic and cloud processing of certified CFA. Fu et al. (2012) determined the dissolution kinetics of CFA samples at pH 2, while Chen and Grassian (2013) investigated the effect of organic species (e.g., oxalate and acetate) at pH 2-3. These studies showed that high acidity and the presence of oxalate enhanced Fe dissolution at the surface of CFA particles, similar to those reported in mineral dust (Chen et al., 2012; Chen and Grassian, 2013; Fu et al., 2012; Ito and Shi, 2016; Shi et al., 2011a). They also demonstrated that there are large differences in dissolution rates in different types of CFA, likely related to Fe speciation.

Furthermore, high ionic strength, commonly seen in aerosol water, affects the activity of molecular species present in solution, consequently it can significantly impact the Fe dissolution behaviour. Recent studies have considered the effect of the high ionic strength on the Fe dissolution kinetics of CFA under acidic conditions. For example, the Fe solubility of CFA samples was measured at pH 1-2 with high sodium chloride (NaCl) concentrations (Borgatta et al., 2016), and with high sodium nitrate ($NaNO_3$) concentrations Kim et al. (2020). In real atmospheric conditions, NaCl or $NaNO_3$ are unlikely to be the main driver of high ionic strength in aged CFA. Although NaCl can coagulate with dust particles in the marine boundary layer (Zhang et al., 2003), the aging of ~~coal fly ash~~CFA is primarily by the uptake of secondary species, particularly ~~sulphate~~ sulfate and ammonia (Li et al., 2003). Ito and Shi (2016) found that at low pH and high concentration of $(NH_4)_2SO_4$ the Fe solubility of mineral dust is likely to be enhanced by the adsorption of ~~sulphate~~ sulfate ions on the particle surface. However, to date the effect of high $(NH_4)_2SO_4$ concentrations on the Fe dissolution behaviour in combustion sources in the presence or absence of oxalate remains unknow.

The dissolution kinetics measured by Chen and Grassian (2013) ~~has~~ have been used to develop a modelled dissolution scheme for CFA, assuming a single Fe-bearing~~Fe~~ phase in CFA (Ito, 2015). However, there are multiple Fe-bearing ~~Fe~~ phases in CFA, primarily hematite, magnetite and Fe in aluminium silicate glass (Brown et al., 2011; Chen et al., 2012; Fu et al., 2012; Kukier et al., 2003; Kutchko and Kim, 2006; Lawson et al., 2020; Sutto, 2018; Valeev et al., 2019; Waanders et al., 2003; Wang, 2014; Zhao et al., 2006), but also accessory Fe-bearing minerals for example silicates, carbonate, ~~sulphides~~ sulfides and ~~sulphates~~ sulfates (Zhao et al., 2006). These phases have a range of reactivities. Previous studies showed that CFA dissolves much faster

during the first 1-2 hours than subsequently (Borgatta et al., 2016; Chen et al., 2012; Chen and Grassian, 2013; Fu et al., 2012; Kim et al., 2020), confirming the existence of multiple Fe-bearing phases within a single CFA sample with ~~large~~different ~~difference in Fe dissolution from different phases~~dissolution behaviour.

In this study, laboratory experiments were conducted to determine the dissolution kinetics of coal combustion ~~sources~~ emission products (~~e.g.,~~i.e., ~~coal fly ash~~CFA) during simulated atmospheric acidic processing in the presence of $(NH_4)_2SO_4$ and oxalate which are commonly found in atmospheric aerosols. In particular, we investigated the effect of high $(NH_4)_2SO_4$ concentrations on the proton-promoted and oxalate-promoted Fe dissolution at low pH conditions. Our study also determined the Fe-bearing ~~Fe~~ phases present in the CFA and compared them to those present in mineral dust. The experimental results enabled us to develop a new Fe release scheme for CFA sources which was then implemented into the global atmospheric chemical transport model IMPACT. The model results were compared with observations of Fe solubility ~~surface concentration of dissolved Fe~~ in aerosol particles over the Bay of Bengal from Bikkina et al. (2020).

2 Materials and Methods

2.1 Sample collection and subsequent size fractionation

CFA samples were collected from the electrostatic precipitators at three coal-fired power stations at different locations: United Kingdom (Aberthaw ash), Poland (Krakow ash), and China (Shandong ash). The bulk samples were resuspended to obtain ~~dust~~ aerosol fractions representative of particles emitted into the atmosphere. A custom-made resuspension system was used to collect the PM_{10} fraction (particles with an aerodynamic diameter smaller than 10 µm), which is shown in Fig. S1. Around 20 g of sample was placed into a glass bottle and injected at regular intervals (2-5 sec) into a glass reactor (~70 L) by flushing the bottle with pure nitrogen. The air in the reactor was pumped at a flow rate of 30 L min^{-1} into a PM_{10} sampling head. Particles were collected on 0.6 µm polycarbonate filters and transferred into centrifuge tubes. The system was cleaned manually and flushed for 10 min with pure nitrogen before loading a new sample. A soil sample from Libya (Soil 5, 32.29237N/22.30437E) was dry sieved to 63 µm ~~(which is referred to as Libya dust)~~ and used as an analogue for a Saharan mineral dust precursor to make a comparison between CFA and mineral dust~~and used for the comparison of CFA with mineral dust~~.

2.2 Fe dissolution kinetics

The Fe dissolution kinetics of the CFA samples ~~was~~ were determined by time-dependent leaching experiments. We followed a similar methodology as in Ito and Shi (2016). PM_{10} fractions were exposed to H_2SO_4 solutions at pH 1, 2 or 3, in the presence of $H_2C_2O_4$ and/or $(NH_4)_2SO_4$ to simulate acidic processing in aerosol conditions. The concentration of $H_2C_2O_4$ in the experiment solutions was chosen based on the molar ratio of oxalate and ~~sulphate~~ sulfate in $PM_{2.5}$ (particles with an aerodynamic diameter smaller than 2.5 µm) from observations over the East Asia region (Yu et al., 2005). Around 50 mg of CFA was leached in 50 ml of acidic solution to obtain a ~~dust~~particles/liquid ratio of 1 g L^{-1}. The sample solution was mixed continuously on a rotary mixer, in the dark at room temperature. A volume of 0.5 mL was sampled at fixed time intervals (2.5, 15, 60 min and 2, 6, 24, 48, 72, and 168 hours after the CFA sample was added to the experiment solution) and filtered through 0.2 µm pore size syringe filters. The dissolved Fe concentration in the filtrate was determined using the ferrozine method (Viollier et al., 2000). Leaching experiments were also conducted on the Libyan dust precursor sample. The relative standard deviation (RSD) at each sampling time varied from 4 % to 15 % (n=7).

The pH of all the experiment solutions was calculated using the E-AIM model III for aqueous solutions (Wexler and Clegg, 2002). In part this was because the high ionic strength generated by the elevated concentration of $(NH_4)_2SO_4$ prevents electrochemical sensors from making accurate pH measurements. For the experiment solutions with no $(NH_4)_2SO_4$, the pH

was measured by a pH meter before adding the ash and at the end of the experiments. The solution pH increased after adding the ash, and the change in pH was used to estimate the buffer capacity of alkaline minerals in the samples, including for example calcium carbonates ($CaCO_3$), lime (CaO), and portlandite ($Ca(OH)_2$). The estimated concentration of H^+ buffered was used to input the concentration of H^+ into the E-AIM model. For each experiment, the pH was calculated before adding the CFA samples and at the end of the experiments. The pH of the original solution before adding the samples was estimated from the molar concentrations (mol L^{-1}) of H_2SO_4, $H_2C_2O_4$ and $(NH_4)_2SO_4$ used to prepare the solution. The model inputs included the total concentrations of H^+ (without $H_2C_2O_4$ contribution), NH_4^+, SO_4^{2-} and $H_2C_2O_4$. For the experiment solutions with no $(NH_4)_2SO_4$, we calculated the final pH by reducing the total H^+ concentration input into the model to match the pH measured at the end of the experiments. The buffered H^+ was then estimated from the difference between the original and final H^+ concentration input into the model. To determine the final pH of the solutions with high ionic strength, the H^+ concentration input in the model was calculated as the difference between the H^+ concentration in the original solution and the buffered H^+ estimated at low ionic strength.

For the solution with no $(NH_4)_2SO_4$, the difference between calculated and measured pH is <7%. Table S1 reports the concentrations of H_2SO_4, $H_2C_2O_4$ and $(NH_4)_2SO_4$ in the experiment solutions, the original and final pH from model estimates (including H^+ concentrations and activities), and the pH measurements for the solution with low ionic strength.

2.3 Sequential extractions

The content of Fe oxide species in the samples was determined by Fe sequential extraction (Baldo et al., 2020; Poulton and Canfield, 2005; Raiswell et al., 2008; Shi et al., 2011b). The Fe oxide species included highly reactive amorphous Fe oxide-hydroxide (FeA), crystalline Fe oxide-hydroxide, mainly goethite and hematite (FeD), and Fe associated with magnetite (FeM).

To extract FeA, samples were leached in an ascorbate solution buffered at pH 7.5 (Raiswell et al., 2008; Shi et al., 2011b). The ascorbate solution contained a deoxygenated solution of 50 g L^{-1} sodium citrate, 50 g L^{-1} sodium bicarbonate, and 10 g L^{-1} of ascorbic acid. Around 30 mg of CFA was leached for 24 hours in 10 mL of ascorbate extractant, mixed continuously on a rotary mixer. The extraction solution was then filtered through a 0.2 µm membrane filter. In order to extract FeD, the residue was leached for 2 more hours in a dithionite solution buffered at pH 4.8 (50 g L^{-1} sodium dithionite in 0.35 M acetic acid and 0.2 M sodium citrate) (Raiswell et al., 2008; Shi et al., 2011b).

For the extraction of FeM, the CFA samples were first leached for 2 hours using a citrate-buffered dithionite solution to remove FeD. The residue collected after filtration was then leached for 6 hours in a solution of 0.2 M ammonium oxalate ($(NH_4)_2C_2O_4$) and 0.17 M $H_2C_2O_4$ at pH 3.2 (Poulton and Canfield, 2005). The Fe extractions were all carried out in the dark at room temperature. The Fe concentration in the filtered extraction solutions was measured using the ferrozine method (Viollier et al., 2000) or by inductively coupled plasma optical emission spectrometry (ICP-OES) analysis for the solutions containing high concentration of oxalate.

The total Fe content in the samples was determined by microwave digestion in concentrated nitric acid (HNO_3) followed by inductively coupled plasma mass spectrometry (ICP-MS) analysis. The recovery of Fe assessed using a standard reference material for urban particulate matter (NIST SRM 1648A) was around 89%. Therefore, the total Fe in the Libyan dust precursor sample could be underestimated somewhat as crystalline aluminium silicate minerals may not be fully digested.

The sequential extraction techniques were tested using the Arizona Test Dust (ATD, Power Technology, Inc.). The RSD% obtained for each extract using the ~~Arizona test dust~~ATD was 3% for FeA, 11% for FeD, 12% for FeM (n=7) and 2% for the total Fe (n=~~7~~3). A summary of the results for the ATD is reported in Table S2.

2.4 X-ray absorption near edge structure (XANES) analysis

We collected XANES spectra to qualitatively examine the Fe speciation in the CFA samples. The XANES spectra at the Fe K-edge were collected at the Diamond Light Source beamline I18. A Si(111) double-crystal monochromator was used in the experiments. The beam size was 400 μm×400 μm. The XANES spectra were collected from 7000 to 7300 eV at a resolution varying from 0.2 eV for 3 s in proximity to the Fe K-edge (7100–7125 eV) to 5 eV for 1 s from 7100 to 7300 eV. Powder samples were suspended in methanol and deposited on Kapton® tape. The analysis was repeated three times. We measured the XANES spectra of the CFA-PM_{10} fractions and mineral standards including hematite, magnetite, and illite. Data were processed using the Athena program, part of the software package Demeter (version 0.9.26) (Ravel and Newville, 2005).

2.5 Model description

This study used the Integrated Massively Parallel Atmospheric Chemical Transport (IMPACT) model (Ito et al., 2021a and references therein). The model simulates the emission, chemistry, transport, and deposition of Fe-containing aerosols and the precursor gases of inorganic and organic acids. The coating of acidic species on the surface of Fe-containing aerosols promotes the release of soluble Fe in the aerosol deliquescent layer and enhances the aerosol Fe solubility (Li et al., 2017). On the other hand, the external mixing of oxalate-rich aerosols with Fe-rich aerosols can suppress the oxalate-promoted Fe dissolution at low concentration of oxalate near the source regions (Ito, 2015). However, the internal mixing of alkaline minerals such as calcium carbonate with Fe-containing dust aerosols can suppress the Fe dissolution (Ito and Feng, 2010). Since CFA particles are co-emitted with acidic species, the transformation of relatively insoluble Fe in coal combustion aerosols into dissolved Fe is generally much faster than that for mineral dust aerosols during their atmospheric lifetime (Ito, 2015; Ito and Shi, 2016). Additionally, the size of CFA particles is substantially smaller than that of mineral dust. Thus, we adopted an observationally constrained parameter for the dry deposition scheme (Emerson et al., 2020) to improve the simulation of dry deposition velocity of fine particles.

To improve the accuracy of our simulations of Fe-containing aerosols, we revised the on-line Fe dissolution schemes in the original model (Ito et al., 2021a) in conjunction with ~~the mineralogy-based emission rates and~~ a more dynamic range of pH estimates. ~~To implement 3-step dissolution schemes, we used the mineral-specific emission inventory for anthropogenic Fe emissions (Rathod et al., 2020).~~ To apply the Fe dissolution schemes for high ionic strength in aerosols, we used the mean activity coefficient for pH estimate (Pye et al., 2020). Moreover, the dissolution rate was assumed to be dependent of pH for highly acidic solutions (pH < 2) unlike in the former dissolution scheme (Ito, 2015), which allowed us to predict the sensitivity of Fe dissolution to pH lower than 2.

To validate the new dissolution scheme, we compared our model results with observations of Fe solubility ~~surface concentration of dissolved Fe~~ in $PM_{2.5}$ aerosol particles over the Bay of Bengal (Bikkina et al., 2020).

3 Experimental results

3.1 Fe dissolution kinetics

We determined that Krakow ash had the largest buffer capacity, around 0.008 moles of buffered H^+ per litre, which was related to the content of alkaline minerals in the sample. The buffer capacity of Aberthaw and Shandong ash was ~10 times smaller than that of Krakow ash, around 0.0007 moles of buffered H^+ per litre. Leaching Krakow ash in 0.005 M H_2SO_4, the initial concentration of H^+ was similar to the concentration of the H^+ buffered. As a result, the solution pH raised from approximatively 2.1 to 2.7 corresponding to a pH change of around 20% (Table S1). For all the other experimental conditions, the pH change was below 12% (Table S1). At the pH conditions used in this study (pH 1-3), acid buffering was fast and likely

occurred within the first 1-2 hours. We assumed that the calculated final pH was representative of the solution pH over the duration of the experiments. The leaching experiments were conducted up to 168 h to better capture the dissolution curve in the kinetic model but also considering the tropospheric lifetime of aerosol particles.

Dissolved Fe at different time intervals is reported as Fe%, which is the fraction of Fe dissolved to the total Fe content (FeT) in the CFA samples. For all samples, a fast dissolution rate was observed at the beginning of the experiment. In the case of Krakow ash, ~~a~~ the dissolution plateau was reached after 2-hour leaching in 0.005 M H_2SO_4 as sufficient Fe may be dissolved from the highly reactive Fe species to suppress the dissolution of less reactive Fe ~~which was likely due to the pH change~~. For that sample/initial condition the pH increased to 2.7, and no more Fe was dissolved, leading to a total Fe solubility of ~9% over the duration of the experiment (7 days) (Fig. 1a). Dissolving Krakow ash in 0.01 M H_2SO_4 (Fig. 1a), the experiment solution had a final calculated pH of 2.1. The total Fe solubility was 34% at pH 2.1, almost 4 times higher than that at pH 2.7 (in 0.005 M H_2SO_4). Dissolution of Aberthaw and Shandong ash was slower compared to Krakow ash (Figs. 1b and 2c, respectively). Leaching Aberthaw and Shandong ash in 0.005 M H_2SO_4 resulted in solutions with a pH of around 2.2. At this pH, the total Fe solubility was 18% for Aberthaw ash and 21% for Shandong ash, which is 9-10 times higher than the total Fe solubility at pH 2.9 (in 0.001 M H_2SO_4), around 2% for both samples.

The experimental treatment of dissolved Fe from Krakow ash in 0.05 H_2SO_4 solution with 1 M $(NH_4)_2SO_4$ (Fig. 1a) resulted in a final predicted pH of 2.1. At that pH, the total Fe solubility of Krakow ash increased from 34% with no $(NH_4)_2SO_4$ to 48% with high $(NH_4)_2SO_4$ concentration. The total Fe solubility of Krakow ash was around 28% at pH 3.0 with 1 M $(NH_4)_2SO_4$ (Fig. 1a), 3 times higher than that at pH 2.7 with no $(NH_4)_2SO_4$. At around pH 2, the total Fe solubility of Aberthaw (Fig. 1b) and Shandong ash (Fig. 1c) increased by around 20% and 30% in the presence of $(NH_4)_2SO_4$. By contrast, the total Fe solubility at pH 3.1 with 1 M $(NH_4)_2SO_4$ was 7.5% for Aberthaw ash (Fig. 1b) and 14% for Shandong ash (Fig. 1c), respectively, which was around 4 and 7 times higher than in the experiments carried out at pH 2.9 without $(NH_4)_2SO_4$.

The Fe dissolution of the CFA samples in H_2SO_4 solutions with 0.01 M $H_2C_2O_4$ (at around pH 2) is shown in Fig. 2. The total Fe solubility of Krakow ash at pH 1.9 with 0.01 M $H_2C_2O_4$ was 61% (Fig. 2a), which was almost 2 times higher than that at pH 2.1 but without $H_2C_2O_4$ (Fig. 2a). For Aberthaw ash, oxalate contribution to the dissolution process led to a total Fe solubility of 30% at pH 2.0 (Fig. 2b), which was 70% higher than in the experiment carried out in 0.005 M H_2SO_4 (~pH 2.2) (Fig. 2b). Shandong ash dissolution behaviour was not affected by the presence of oxalate (Fig. 2c).

We also investigated the effect of high $(NH_4)_2SO_4$ concentration on oxalate-promoted dissolution. In Fig. 2a, the total Fe solubility of Krakow ash decreased from 61% at pH 1.9 in the presence of oxalate to 54% at pH 2.0 with oxalate and $(NH_4)_2SO_4$. For Aberthaw ash, the total Fe solubility at pH 2.0 decreased from 30% in the presence of oxalate to 19% after the addition of $(NH_4)_2SO_4$ (Fig. 2b).

Figure 3 shows the Fe dissolution behaviour of Krakow ash at different pH conditions in the presence of 1 M $(NH_4)_2SO_4$ and $H_2C_2O_4$ (0.01-0.03 M depending on the solution pH). The total concentration of oxalate ions was calculated using the E-AIM model and was similar at different pH conditions, 0.015 at pH 1.0 (Experiment 7 Table ~~S2~~S3), 0.009 at pH 2.0, and 0.01 at pH 2.9 (Experiments 3 Table ~~S2~~S3). The highest total Fe solubility was observed at pH 1.0 (~67%). At pH 2.0, the total Fe solubility decreased to 54%, and no substantial variations were observed between pH 2.0 and pH 2.9 (54%-51%). At pH 1.0, the concentration of H^+ was considerably higher compared to pH 2.0-2.9, leading to a faster dissolution rate. The total concentration of oxalate ions was 1.5-1.6 times higher in the solution at pH 1.0 than at pH 2.0-2.9, which may also contribute to the faster dissolution rate. $C_2O_4^{-2}$ concentration increased with rising pH. Although the concentration of H^+ was lower at pH 2.9 than at pH 2.0, the E-AIM model estimated that $C_2O_4^{-2}$ contributed around 35% of the total oxalate concentration at pH 2.9, which was 4.5 times higher than at pH 2.0 (Experiments 3 Table ~~S2~~S3). The similar dissolution behaviour at pH 2.0 and

pH 2.9 conditions may reflect the combination of these two opposite factors, higher concentration of $C_2O_4^{-2}$ but lower concentration of H^+ at pH 2.9 compared to 2.0.

We determined the Fe dissolution behaviour of Krakow ash at pH 1.0 in the presence of oxalate and increasing concentrations of $(NH_4)_2SO_4$. The ash was leached in H_2SO_4 solutions with 0.03 M $H_2C_2O_4$ at pH 1.0, while the concentration of $(NH_4)_2SO_4$ varied from 0 to 1.5 M. In Fig. 4, the total Fe solubility of Krakow ash in the presence of oxalate was 75% at pH 1.0 and decreased to 68% after the addition of 0.5 M $(NH_4)_2SO_4$. Higher $(NH_4)_2SO_4$ concentrations did not affect the Fe dissolution behaviour in the presence of oxalate at pH 1.0.

3.2 Fe speciation

The Fe-bearing ~~Fe~~ phases in the CFA samples determined through sequential extractions are shown in Fig. 5c. The Fe speciation in the ~~Saharan~~ Libyan dust precursor ~~sample~~ is added for comparison. Krakow ash had a total Fe (FeT) content of 5.2%, while FeT in Aberthaw and Shandong ash was 3.1% and 1.6% respectively. Amorphous Fe (FeA/FeT) was 6.5% in Krakow ash, 2% in Aberthaw ash, and 4.6% in Shandong ash. The CFA samples showed very different dithionite Fe (FeD/FeT) content, 21.5% in Krakow ash, 8% in Aberthaw ash and 14.8% in Shandong ash. The content of magnetite (FeM/FeT) was considerably higher in Krakow ash (22.4%) compared to Aberthaw (2.9%) and Shandong (4.5%) ash. About 50 %–87 % of Fe was contained in other phases most likely in aluminosilicates. Overall, CFA had more magnetite and highly reactive amorphous Fe and less dithionite Fe than the Libyan dust precursor sample.

In Figs. ~~S2~~5a-b, the Fe K-edge XANES spectra of Krakow and Aberthaw ash showed a single peak in the pre-edge region at around 7114.3 eV and 7114.6 eV, respectively. In the edge region, Aberthaw ash showed a broad peak at around 7132.2 eV, while the peak of Krakow ash was slightly shifted to 7132.9 eV and narrower. The pre-edge peak at around 7115.4 suggests that Fe was mainly as Fe(III). The spectral features of Aberthaw and Krakow ash are different from those of the hematite, magnetite and illite standards suggesting that the glass fraction was dominant and controlled their spectral characteristics, which is consistent with the results of the Fe sequential extractions. The XANES Fe K-edge spectra of the CFA samples have some common features with those of Icelandic dust but tend to differ from mineral dust sourced in the Saharan dust source region. In the pre-edge region of the spectrum, Icelandic dust (sample D3 in Figs. 5a-b) showed a main peak at around 7114.4 eV and a second less intense peak at around 7112.7 eV, while a broad peak was observed at around 7131.9 eV in the edge region (Baldo et al., 2020). A mineral dust sample from western Sahara (WS dust in Figs. 5a-b) showed a distinct double peak in the pre-edge region at around 7113.9 and 7115.2 eV, and a main peak in the edge region at around 7133.3 eV (Baldo et al., 2020).~~The XANES Fe K-edge spectra of the CFA samples have some common features with those of Icelandic dust, but differs from northern African dust (Fig. S2). Aluminium silicate glass is also dominant in Icelandic dust (Baldo et al., 2020). In the pre-edge region, Icelandic dust (sample MIR 45 in Fig. S2) showed a main peak at around 7114.4 eV and a second less intense peak at around 7112.7 eV, while a broad peak was observed at around 7131.9 eV in the edge region (Baldo et al., 2020). Northern African dust (western Sahara in Fig. S2) showed a distinct double peak in the pre-edge region at around 7113.9 and 7115.2 eV, and a main peak in the edge region at around 7133.3 eV (Baldo et al., 2020).~~ The similarities between Icelandic ash and CFA could be because aluminium silicate glass is dominant in these samples (e.g., Baldo et al., 2020; Brown et al., 2011), while Fe-bearing phases in mineral dust from the Saharan region are primarily iron oxides minerals such as hematite and goethite, clay minerals and feldspars (e.g., Shi et al., 2011b).

Field Code Changed

Field Code Changed

Field Code Changed

Field Code Changed

Formatted: English (United Kingdom)

4 Fe simulation from the IMPACT model

4.1 Fe dissolution scheme

Based on the laboratory experiments carried out on the CFA samples, we implemented a 3-step dissolution scheme for proton-promoted and oxalate-promoted Fe dissolution (Table 1). The Fe dissolution kinetics ~~was~~ were described as follows (Ito, 2015):

$$\sum_i RFe_i = k_i(pH,T) \times a(H^+)^{m_i} \times f_i \quad (1)$$

where RFe_i is the dissolution rate of individual mineral i, k_i is the rate constant (moles Fe g^{-1} s^{-1}), $a(H^+)$ is the H^+ activity in solution, m_i represents the empirical reaction order for protons. The function f_i ($0 \leq f_i \leq 1$) accounts for the suppression of mineral dissolution by competition for oxalate between surface Fe and dissolved Fe (Ito, 2015):

$$f_i = 0.17 \times \ln([\text{lig}] \times [Fe]^{-1})_i + 0.63 \quad (2)$$

in which, [Fe] is the molar concentration (mol L^{-1}) of Fe^{3+} dissolved in solution, and [lig] is the molar concentration of ligand (e.g., oxalate). f_i was set to 1 for the proton-promoted dissolution.

The scheme assumes 3 rate constants "fast", "intermediate" and "slow" for the proton-promoted, and the proton + oxalate-promoted dissolution (Table 1). These were obtained by fitting the parameters to our measurements for Krakow ash in H_2SO_4 and $(NH_4)_2SO_4$ at pH 2-3, with and without oxalate (Experiments 2 and 3 in Table S1), which are shown in Fig. 6. The fast rate constant represents highly reactive Fe species such as amorphous Fe oxyhydroxides, Fe carbonates and Fe ~~sulphates~~sulfates. The intermediate rate constant can be applied to nano-particulate Fe oxides, while more stable phases including for example Fe-aluminosilicate and crystalline Fe oxides have generally slower rates (Ito and Shi, 2016; Shi et al., 2011a; Shi et al., 2011b; Shi et al., 2015). Similarly, we predicted the dissolution kinetics of Aberthaw ash and Shandong ash (Figs. ~~7~~S3-S5). The dissolution kinetics of Krakow ash were~~as~~ calculated based also on the experimental results at pH 1.0, which is shown in Fig. ~~S6~~ S2 in comparison with kinetics predicted at pH 2.0 and pH 2.9 conditions.

The contribution of the oxalate-promoted dissolution to dissolved Fe was derived as the difference between the estimated dissolution rates for the proton + oxalate-promoted dissolution and the proton-promoted dissolution:

$$RFe_{i(oxalate)} = RFe_{i(proton\ +\ oxalate)} - RFe_{i(proton)} \quad (3)$$

The Fe dissolution rates were predicted at a wider range of pH using Eq. (1) and Eq. (3) and the parameters in Table 1:

$$RFe_i = RFe_{i(proton\ +\ oxalate)} \text{ when } RFe_{i(oxalate)} < 0 \quad (4)$$

Since $RFe_{i(oxalate)}$ is less than 0 at low pH (< 2), this equation applies to highly acidic conditions. As a result, the predicted amount of dissolved Fe was smaller when using the dissolution rate for the proton + oxalate-promoted dissolution, $RFe_{i(proton\ +\ oxalate)}$, rather than the rate for the proton-promoted dissolution, $RFe_{i(proton)}$, at pH < 2. Accordingly, the dissolution rate, RFe_i, was less dependent on the pH compared to $RFe_{i(proton)}$ at highly acidic conditions, possibly due to the competition for the formation of surface complexes.

At pH > 2 when oxalate does promote Fe dissolution, the following equation applies:

$$RFe_i = RFe_{i(proton)} + RFe_{i(oxalate)} \text{ when } RFe_{i(oxalate)} > 0 \quad (5)$$

4.2 Aerosol ~~Surface concentration of dissolved Fe~~Fe solubility over the Bay of Bengal

The new dissolution scheme was applied in the IMPACT atmospheric chemistry transport model to predict the Fe solubility ~~surface concentration of dissolved Fe~~ in atmospheric particles collected over the Bay of Bengal, which is an area for which there are detailed field measurements available (Bikkina et al., 2020; Kumar et al., 2010; Srinivas and Sarin, 2013; Srinivas et al., 2012) and multi-modelling analyses have been done (Ito et al., 2019). It thus represents a test for our experimental results in actual field conditions. Three sensitivity simulations were performed to explore the effects of the uncertainties associated with the dissolution schemes and mineralogical component of Fe. In addition, the former setting (Ito et al., 2021a) was used in the IMPACT model for comparison.

For all simulations, ~~In sensitivity Test 0, t~~the total Fe emissions from anthropogenic combustion sources and biomass burning ~~emission in anthropogenic aerosols was~~were estimated using ~~Fe emission~~the Fe emission inventory of Ito et al. (2018) including also emissions from the iron and steel industry, whereas Fe emissions from mineral dust sources were dynamically simulated (Ito et al., 2021a). ~~factors by each sector such as energy, heavy industry, and iron and steel industry for the simulation years (Ito et al., 2018), whereas in sensitivity Test 1, Test 2, and Test 3, the mineral specific emission inventory for the year 2010 by Rathod et al. (2020) was used.~~ In Test 0, we ran the model without the upgrades of the dissolution scheme discussed in section 2.4, and apply in addition the photoinduced dissolution scheme for both combustion and dust aerosols (Ito, 2015; Ito and Shi, 2016), which was turned off in Test 1, Test 2, and Test 3 due to the lack of laboratory measurements under high ionic strength. To estimate the aerosol pH, we applied a H^+ activity coefficient of 1 for Test 0, while the mean activity coefficient from Pye et al. (2020) was used for the other tests. The dissolution rate was assumed as pH-independent for highly acidic solutions (pH < 2) (Ito, 2015) in Test 0, based on the laboratory measurements in Chen et al. (2012), while no pH threshold was considered in Test 1, Test 2, and Test 3 as the total dissolution (proton + oxalate) was suppressed at pH < 2 from the predicted dissolution rate.

In Test 1, we used the new dissolution scheme accounting for the proton- and oxalate- promoted dissolution of Krakow ash for all combustion aerosols in the model (Table 1). The dissolution kinetics ~~was~~ were calculated using the ~~mineral specific inventory~~base mineralogy for anthropogenic Fe emissions reported in Table S11 of Rathod et al. (2020). The Fe composition of wood was used for open biomass burning (Matsuo et al., 1992). In this simulation, ~~3~~ three Fe pools were considered. ~~Sulphate~~ Sulfate Fe in Rathod et al. (2020) was assumed as fast pool, magnetite Fe as intermediate pool, hematite, goethite and clay~~Fe aluminosilicate~~ as slow pool. In Test 2, we calculated the dissolution kinetics only considering the proton-promoted dissolution. In Test 3, the Fe pools were as determined here for Krakow ash: ascorbate Fe (FeA) as fast pool, magnetite Fe (FeM) as intermediate pool, hematite plus goethite Fe (FeD) and other Fe as slow pool (Fig. 5). FeA contains highly reactive Fe species with fast dissolution rates (Raiswell et al., 2008; Shi et al., 2011b). FeM appeared to work well for the different fly ash samples in the dissolution scheme as intermediate Fe pool. FeD is associated with crystalline Fe oxides ~~and a predominant proportion of this is~~which are mostly highly insoluble (Raiswell et al., 2008; Shi et al., 2011b), thus it was considered as slow pool in the dissolution scheme. We assumed other Fe to be mostly ~~as~~ Fe-bearing aluminosilicates and considered this as slow Fe pool.

~~The temporally and regionally averaged, model-calculated surface concentration of aerosol Fe (Fig. 7), dissolved Fe (Fig. 8) and Fe solubility (Figs. 9 and S7) for the fine mode ($PM_{2.5}$) along the cruise tracks were compared with the measurements over the Bay of Bengal for the period extending from 27 December 2008 to 26 January 2009 (Bikkina et al., 2020).~~ Observations of total Fe concentration and Fe solubility in $PM_{2.5}$ along the cruise tracks over the Bay of Bengal for the period extending from 27 December 2008 to 26 January 2009 (Bikkina et al., 2020) were compared with temporally and regionally averaged data from model estimates. The daily averages of model results were calculated from hourly mass concentrations in the air over the surface ocean along the cruise tracks. The ~~average aerosol Fe~~ concentration of total Fe observed over the Bay of

Bengal ~~varies~~ varies from 145 ± 144 ng m^{-3} over the North Bay of Bengal (27 December 2008 - 10 January 2009) to 55 ± 23 ng m^{-3} over the South Bay of Bengal (11-26 January 2009) (Bikkina et al., 2020). In Fig. ~~7~~8, the modelled ~~aerosol Fe~~ concentrations of total Fe exhibit a similar variability to that of measurements with relatively higher values over the North Bay of Bengal (~~101~~ 59 ± ~~57~~ 29 ng m^{-3} in ~~Test 0, and 81 ± 37 ng m^{-3} in Test 1-3~~different sensitivity simulations) compared to the South Bay of Bengal (~~21~~ 20 ± 1~~2~~3 ng m^{-3} in different sensitivity simulations~~in Test 0, and 34 ± 25 ng m^{-3} in Test 1- 3~~). However, the modelled concentrations of total Fe were underestimated by a factor of 2.9 ± 1.5. The model reproduced the source apportion of Fe (Fig. ~~7~~8 - Table S4) which is qualitatively derived from previous observational studies indicating that the ~~aerosol Fe~~ concentrations of total Fe in aerosols over the North Bay of Bengal are influenced by emissions of dust and combustion sources from the Indo-Gangetic Plain (Kumar et al., 2010), whereas combustion sources (e.g., biomass burning and fossil-fuel) from South-East Asia are dominant over the South Bay of Bengal (Kumar et al., 2010; Srinivas and Sarin, 2013). On the other hand, the model could not reproduce the peak in total Fe concentration (1.8% of Fe content in $PM_{2.5}$ sample) reported around 29 December 2008. The total Fe observed in PM_{10} (430 ng m^{-3}) on 29 December 2008 is lower than that measured on the day before (667 ng m^{-3}) and the day after (773 ng m^{-3}), whereas that in $PM_{2.5}$ peaked on 29 December 2008 (Srinivas et al., 2012). Thus, the extreme value recorded only for $PM_{2.5}$ on this date may be an outlier.~~The total Fe observed in $PM_{2.5}$ (613 ng m^{-3}) is higher than that in PM_{10} (430 ng m^{-3}) (Srinivas et al., 2012). This may be due to the measurement uncertainty including sample collection with two different high-volume samplers (Kumar et al., 2010).~~

The comparison of Fe solubility using the same total Fe emissions directly represents the effect of the new dissolution scheme on $PM_{2.5}$.

~~The average aerosol dissolved Fe concentration measured over the North Bay of Bengal (16 ± 9 ng m^{-3}) is slightly lower than that over the South Bay of Bengal (18 ± 10 ng m^{-3}) (Bikkina et al., 2020). The model prediction of dissolved Fe over the North Bay of Bengal was 6 ± 2 ng m^{-3} Fe in Test 0, 21 ± 10 ng m^{-3} in Test 1, and 31 ± 28 ng m^{-3} in Test 2, and 13 ± 10 ng m^{-3} in Test 3. The aerosol dissolved Fe estimated over the South Bay of Bengal was 6 ± 1 ng m^{-3} in Test 0, 15 ± 10 ng m^{-3} in Test 1, 32 ± 22 ng m^{-3} in Test 2, and 12 ± 7 ng m^{-3} in Test 3. In Fig. 8, our model results show that the contribution of mineral dust to aerosol dissolved Fe was higher over the North Bay of Bengal (14% ± 6% in Test 1, 28% ± 34% in Test 2, and 33% ± 26% in Test 3) compared to the South Bay of Bengal (3% ± 1% in Test 1, 1% ± 1% in Test 2, and 3% ± 1% in Test 3). Overall, anthropogenic combustion sources were dominant over the Bay of Bengal accounting for 84% ± 12% in Test 1, 72% ± 29% in Test 2, and 69% ± 24% in Test 3 of the aerosol dissolved Fe. Moreover, after 22 January 2009, the contribution of open biomass burning sources increased up to 47% in Test 1, 64% in Test 2, and 60% in Test 3 (Fig. 8).~~

The aerosol Fe solubility measured over the South Bay of Bengal is higher than that over the North Bay of Bengal, respectively 32% ± 11% and 15% ± 7% (Bikkina et al., 2020), and model estimates showed a similar trend (Fig. S~~7~~9). In Fig. S~~7~~9 and Table S5, the calculated ~~average~~ Fe solubilities~~y~~ over the North Bay of Bengal in Test 1 (11% ± 4%), Test 2 (17% ± 5%), and Test 3 (17% ± 6%) ~~in Test 3 (18% ± 10%)~~ wereas ~~as~~ in good agreement with observations.~~, while lower Fe solubility was estimated in Test 0 (8% ± 5%) and higher values were obtained for Test 1 (28% ± 8%).~~ The aerosol Fe solubility over the South Bay of Bengal was better captured in Test 1 (30~~43~~% ± 5~~4~~%) and Test 3 (3~~7~~9% ± 7%), whereas Test 0 showed higher variability (3~~7~~8% ± 22%). The proton-promoted dissolution scheme in Test 2 significantly overestimated the Fe solubility over the Bay of Bengal (Fig. 9 and Table S5~~Figs. 9 and S7~~). The aerosol Fe solubility was largely overestimated in all scenarios after 22 January 2009, as open biomass burning sources become dominant (Fig. 8 and Table S4).

The comparison between observations and model predictions of aerosol Fe solubility over the Bay of Bengal is shown in Fig. ~~9~~S3. The agreement between measurements and model predictions was the best in Test 1 and Test 3. These exhibited good correlation with observations (R = 0.~~60~~ 49 in Test 1 and R = 0.~~51~~ 54 in Test 3), and the lowest ~~centred~~ root ~~-~~mean ~~-~~squared

Formatted: Subscript

~~(RMS)~~ difference between the simulated and observed ~~aerosol~~ Fe solubilities (RMSE = 1~~1~~6 in Test 1 and RMSE = 1~~2~~4 in Test 3). In Test 0, the model estimates showed ~~higher~~ a greater difference from observations (RMSE = 2~~2~~1) and poor correlation (R = 0.2~~63~~0).

5 Discussion

5.1 Dissolution behaviour of Fe in CFA

In this study, the Fe dissolution kinetics of CFA samples from UK, Poland and China ~~was~~ were investigated under simulated atmospheric acidic conditions. A key parameter in both the atmosphere and the simulation experiments is the pH of the water interacting with the CFA particles. The lower the pH of the experimental solution the faster the dissolution and eventually the higher the amount of Fe dissolved. Our results showed a strong pH dependence in low ionic strength conditions, with higher dissolution rates at lower pH. For example, reducing the solution pH from 2.7 to 2.1, the Fe solubility of Krakow ash in H_2SO_4 only increased by a factor of 4 (Fig. 1a) over the duration of the experiments, while the Fe solubility of Aberthaw and Shandong ash increased by 9-10 times from pH 2.9 to pH 2.2 (Figs. 1b-c). This enhancement is higher than that observed in studies conducted on mineral dust samples, which showed that one pH unit can lead to 3-4 times difference in dissolution rates (Ito and Shi, 2016; Shi et al., 2011a). Furthermore, Chen et al. (2012) reported that the Fe solubility of the certified CFA 2689 only increased by 10% from pH 2 to pH 1, after 50 hours of dissolution in acidic media. The Fe solubility of CFA (PM_{10} fractions) after 6 hours at pH 2 was 6%-10% for Aberthaw and Shandong ash respectively, and 28% for Krakow ash (Fig. 1). The Fe in our CFA samples initially dissolved faster than those used by Fu et al. (2012)~~These values are higher than the Fe solubilities measured by Fu et al. (2012)~~, who reported 2.9%-4.2% Fe solubility in bulk CFA from three coal-fired power plants in China after 12-hour leaching at pH 2. ~~This suggest that Fe in our CFA samples initially dissolved faster than those used in Fu et al. (2012). The Fe solubility after 72-hour leaching in H_2SO_4 at around pH 2 varied from around 12% and 17% (Aberthaw and Shandong ash) to 34% (Krakow ash). These values are at the lower end of the range or below those reported in Chen et al. (2012), who measured a Fe solubility of ~20%-70% in certified CFA samples after accumulated acid dissolution of 72 hours at pH 2.~~ These results suggest that there are considerable variabilities in the pH dependent dissolution of Fe in CFA. This could be due to differences in the Fe speciation between CFA samples and/or the different leaching media used.

Our results showed that high ionic strength has a major impact on dissolution rates of CFA at low pH (i.e., pH 2-3). The Fe solubility of CFA increased by approximatively 20%-40% in the presence of 1 M $(NH_4)_2SO_4$ at around pH 2 over the duration of the experiments, and by a factor from 3 to 7 at around pH 3 conditions (Fig. 1). At high ionic strength, the activity of ions in solution is reduced, thus, in order to maintain similar pH conditions, the H^+ concentration has to be increased (Table S1). Although Fe dissolution was primarily controlled by the concentration of H^+, the high concentration of ~~sulphate~~ sulfate ions could also be ~~also~~ an important factor contributing to Fe dissolution, in particular when the concentration of H^+ in the system was low (e.g., pH 3). Previous research found that the high ability of anions to form soluble complexes with metals can enhance Fe dissolution (Cornell et al., 1976; Cornell and Schwertmann, 2003; Furrer and Stumm, 1986; Hamer et al., 2003; Rubasinghege et al., 2010; Sidhu et al., 1981; Surana and Warren, 1969). ~~Sulphate~~ Sulfate ions adsorbed on the particles surface form complexes with Fe (e.g., Rubasinghege et al., 2010). This may increase the surface negative charge favouring the absorption of H^+ and thereby increase ~~the dissolution rate~~Fe dissolution at the particle surface. In addition, the formation of surface complexes may weaken the bonds between Fe and the neighbouring ions (Cornell et al., 1976; Furrer and Stumm, 1986; Sidhu et al., 1981). Cwiertny et al. (2008) reported that at pH 1-2 the high ionic strength generated by NaCl up to 1 M did not influence Fe dissolution of mineral dust particles. However, Ito and Shi (2016) showed that the high ionic strength resulting from the addition of 1 M $(NH_4)_2SO_4$ in leaching solutions at pH 2-3 enhanced the Fe dissolution of dust particles, which was also observed here for the CFA samples. Borgatta et al. (2016) compared the Fe solubility of CFA from USA

Field Code Changed
Field Code Changed
Formatted: Italian (Italy)
Field Code Changed

Midwest, North-East India, and Europe in acidic solution (pH 1-2) containing 1 M NaCl. The Fe solubility measured after 24 hours varied from 15% to 70% in different CFA (bulk samples) at pH 2 with 1 M NaCl, which was considerably higher than that observed at pH 2 with 1 M $NaNO_3$ (<20%) (Kim et al., 2020). Both studies did not investigate the impact of ionic strength on the dissolution behaviour, i.e., by comparing the dissolution at low and high ionic strength. Note that both studies did not specify how the pH conditions were maintained at pH 2. Here, we considered the most important sources of high ionic strength in aerosol water and simulated Fe dissolution in the presence of $(NH_4)_2SO_4$ and $H_2C_2O_4$ under acidic conditions. We emphasize that the pH under high ionic strength here is estimated from a thermodynamic model, similar to those implemented in the IMPACT model.

The presence of oxalate enhanced Fe dissolution in Krakow and Aberthaw ash but not in Shandong ash at around pH 2 (Fig. 2). The effect of oxalate on the Fe dissolution kinetics has also been studied by Chen and Grassian (2013) at pH 2 (11.6 mM $H_2C_2O_4$). After 45-hour leaching, the Fe solubility of the certified CFA 2689 increased from 16% in H_2SO_4 at pH 2 to 44% in $H_2C_2O_4$ at the same pH (Chen and Grassian, 2013). Therefore, the enhancement in Fe solubility of CFA in the presence of oxalate observed in this study (from no impact in Shandong ash to doubled dissolution in Krakow ash) is lower than the 2.8 time increase in Fe solubility reported ~~that reported~~ for the certified CFA 2689 ~~which was around by 2.8 times~~ (Chen and Grassian, 2013). Since no data are available in Chen and Grassian (2013), we are unable to make a comparison with the other two certified CFA samples. The Fe solubility of Krakow ash after 48-hour leaching at pH 1.9 with 0.01 M $H_2C_2O_4$ (Fig. 2a) was 53%, which is within the range of Fe solubilities observed in Chen and Grassian (2013) for the certified CFA samples at similar pH and $H_2C_2O_4$ concentrations (from 44% to 78%), whereas the Fe solubility of Aberthaw and Shandong ash (Figs. 2b-c, 18%-17% after 48-hour leaching at pH 2.0 with 0.01 M $H_2C_2O_4$) was considerably lower than that of certified CFA (Chen and Grassian, 2013). These results suggest a large variability in the effects of oxalate on the Fe dissolution rates in different types of CFA.

Our results also indicated that high $(NH_4)_2SO_4$ concentrations suppress oxalate-promoted Fe dissolution of CFA (Fig. 2), which was not considered in previous research. At pH 1.9 in the presence of oxalate, the Fe solubility of Krakow ash decreased by around 10% after the addition of $(NH_4)_2SO_4$, while the Fe solubility of Aberthaw ash decreased by 35% (Fig. 2). We used the E-AIM model to estimate the concentration of oxalate ions and their activity (Table ~~S2~~S3). The pH influences the speciation of $H_2C_2O_4$ in solution (e.g., Lee et al., 2007). $H_2C_2O_4$ is the main species below pH 2, whereas $HC_2O_4^-$ is dominant between pH ~~1~~2-4. Above pH 4, $C_2O_4^{-2}$ is the principal species. In our experiments, $H_2C_2O_4$ is mainly as $HC_2O_4^-$ at around pH 2 (Experiments 3-4 in Table ~~S2~~S3). In the presence of $(NH_4)_2SO_4$, the activity coefficient of $HC_2O_4^-$ was reduced by approximatively 35-38% (Experiments 3 in Table ~~S2~~S3). Increasing the ionic strength lowers the activity of the oxalate ions, but at the same time favours the dissociation of the acid. At around pH 2 conditions, the E-AIM model estimated that the activity of $C_2O_4^{-2}$ was reduced by around one order of magnitude in the presence of $(NH_4)_2SO_4$, while its concentration increased 12-15 times (Experiments 3 in Table ~~S2~~S3). The adsorption of anions can reduce oxalate adsorption on the particle surface due to electrostatic repulsion which results in slower ~~dissolution rates~~release of Fe (Eick et al., 1999). Precipitation of ammonium hydrogen oxalate ($NH_4HC_2O_4$) can also occur in the system, but this is very soluble and easily re-dissolves forming soluble oxalate species (Lee et al., 2007). We speculate that the high concentration of ~~sulphate~~ sulfate ions is likely to be responsible for inhibiting the oxalate-promoted dissolution by reducing oxalate adsorption on the particle surface. At pH 1 in the presence of oxalate, increasing the concentration of $(NH_4)_2SO_4$ from 0.5 M to 1.5 M did not affect the Fe dissolution behaviour of the CFA samples (Fig. 4). As previously discussed, the adsorption of ~~sulphate~~ sulfate ions on the particle surface may inhibit oxalate-promoted dissolution. However, once the saturation coverage is reached, increasing the concentration of anions has no further effect on the dissolution rate (Cornell et al., 1976).

Fe speciation is an important factor affecting the Fe dissolution behaviour. CFA particles have very different chemical and physical properties depending for example on the nature of coal burned, combustion conditions, cooling process and particle control devices implemented at the power stations (e.g., Blissett and Rowson, 2012; Yao et al., 2015). This is likely the reason why the Fe speciation observed in the CFA samples analysed in this study from different locations varied considerably (Fig. 5). In the CFA samples, the Fe dissolution curves for different pH and ionic strengths generally showed the greatest rate of Fe release within the first 2 hours, followed by a slower dissolution, reaching almost a plateau at the end of the experimental run. This indicates the presence of multiple Fe-bearing ~~Fe~~ phases in CFA particles with a wide range of reactivity. Initially, highly reactive phases were the main contribution to dissolved Fe. As the dissolution continued, ~~more stable~~more refractory ~~-~~phases became the dominant source of dissolved Fe (Shi et al., 2011a). SEM analysis conducted on CFA samples showed that CFA particles are mostly spherical (e.g., Chen et al., 2012; Dudas and Warren, 1987; Valeev et al., 2018; Warren and Dudas, 1989) with Fe oxide aggregates on the surface (Chen et al., 2012; Valeev et al., 2018). The analysis of the CFA samples processed in aqueous solution at low pH suggests that initially Fe dissolved from the reactive external glass coating (Dudas and Warren, 1987; Warren and Dudas, 1989) and from the Fe oxide aggregates on the particle surface (Chen et al., 2012; Valeev et al., 2018). Subsequently, Fe is likely realised from the structure of the aluminium silicate glass (Chen et al., 2012; Dudas and Warren, 1987; Valeev et al., 2018; Warren and Dudas, 1989), and crystalline Fe oxide phases (Warren and Dudas, 1989). Overall, Krakow ash showed the fastest dissolution rates, but the dissolution of highly reactive Fe species as FeA is insufficient to account for the high Fe solubility observed at low pH. Our results showed that once the FeA dissolved, additional Fe was dissolved from more refractory Fe-bearing ~~Fe~~ phases. The modelled dissolution kinetics obtained using FeM as intermediate pool were in good agreements with measurements (Figs. ~~S3~~7-S2~~6~~). FeM is likely to be primary magnetite but may contain a fraction of the more reactive aluminosilicate glass. Our model results suggest that magnetite in CFA particles may be more soluble than has been shown in Marcotte et al. (2020). It is possible that in real CFA samples the ~~mineral~~ physicochemical properties of minerals including for example crystal size, degree of crystallinity, cationic and anionic substitution in the lattice which influence the Fe dissolution behaviour (e.g., Schwertmann, 1991) are likely to be different from those of the reference minerals analysed in Marcotte et al. (2020). In order to investigate the links between Fe solubility and Fe speciation/mineralogy~~In order to estimate in detail the relative contribution of different mineral phases to dissolved Fe~~, more work is needed to determine the Fe mineralogy in CFA samples at emission and after atmospheric processing, in combination with solubility experiments~~most detailed work would be needed to determine Fe mineral phases in pristine and processed CFA particles.~~.

Finally, the modelled dissolution kinetics obtained using the new dissolution scheme for CFA (Table 1) showed better agreement with laboratory measurements than when using the original scheme (Ito, 2015) (Figs~~. S8 and S9~~10). In Figs. ~~S8~~10a-b, we compared the Fe dissolution kinetics of Krakow ash at around pH 2 and 3 with 1 M $(NH_4)_2SO_4$ calculated using the proton-promoted dissolution scheme in Table 1 with the dissolution kinetics calculated at similar pH but using the proton-promoted dissolution scheme for combustion aerosols in Ito (2015) (Table ~~S3~~S6). The dissolution scheme in Ito (2015) was based on laboratory measurements conducted at low ionic strength (Chen et al., 2012) and assumed a single Fe-bearing ~~Fe~~ phase in combustion aerosol particles, while the new dissolution scheme considered the high ionic strength of aerosol water and assumed three rate constants, for fast, intermediate and slow kinetics of the different Fe-bearing ~~Fe~~ phases present in CFA particles. The Fe dissolution kinetics obtained using the new dissolution scheme showed a better agreement with measurements and was enhanced compared to the model estimates obtained using the original dissolution scheme (Ito, 2015) for low ionic strength conditions (Figs. ~~S8~~10a-b). Figures ~~S9~~ 10c-d show~~s~~ the Fe dissolution kinetics of Krakow ash at pH 2.0 and 2.9 with 0.01 M $H_2C_2O_4$ and 1 M $(NH_4)_2SO_4$ calculated using the proton- and oxalate-promoted dissolution scheme in Table 1 and the dissolution kinetics calculated at similar pH and $H_2C_2O_4$ concentration but using the scheme in Ito (2015) (i.e., single phase dissolution, see Table ~~S3~~S6). The Fe dissolution kinetics predicted using the new dissolution scheme had a much better

agreement with measurements. Figure ~~S9c~~ 10e shows the suppression of the oxalate-promoted dissolution at pH 2.0 and high $(NH_4)_2SO_4$ concentrations. At pH 2, the proton-promoted dissolution was comparable to the proton + oxalate-promoted dissolution (Fig. ~~S9c~~10e), with $RFe_{(oxalate)}$ close to zero (see Eq. 3). At pH 2.9, the proton + oxalate-promoted dissolution was higher than the proton + oxalate-promoted dissolution (Fig. ~~S9d~~10f), with $RFe_{(oxalate)} > 0$ (Eq. 5).

Moreover, the new 3-step dissolution scheme better captured the initial fast dissolution of CFA (Fig~~s~~. ~~2 3~~10) which was also observed in previous research (Borgatta et al., 2016; Chen et al., 2012; Chen and Grassian, 2013; Fu et al., 2012; Kim et al., 2020) (except for the certified CFA 2689 in Chen et al. (2012) which showed increasing dissolution rates over the duration of the experiment). Furthermore, the new scheme enabled us to account for the different Fe speciation determined in the CFA samples, which could be a key factor contributing to the different Fe dissolution behaviour observed in the present study and in literature (Borgatta et al., 2016; Chen et al., 2012; Chen and Grassian, 2013; Fu et al., 2012; Kim et al., 2020). In Fig~~s~~. ~~S3-S5~~7, the dissolution kinetics of Aberthaw and Shandong ash calculated using the dissolution rates in Table 1 and the Fe-bearing ~~Fe~~ phases determined in the samples showed a good agreement with measurements.

5.2 Comparison with mineral dust

High ionic strength also impacted the dissolution rates of the ~~Saharan~~ Libyan dust precursor ~~-~~sample at low pH (Fig. ~~S10~~S4). At around pH 2 conditions, the proton-promoted Fe dissolution of Libyan dust ~~Libya dust~~ was enhanced by ~40% after the addition of $(NH_4)_2SO_4$. At around pH 2 and with 0.01 M $H_2C_2O_4$, the Fe solubility of Libyan dust ~~Libya dust~~ decreased by ~30% in the presence of $(NH_4)_2SO_4$. Overall, the Fe solubility of ~~-~~Libyan dust ~~Libya dust~~ was lower compared to that observed in the CFA samples. After 168 hour-leaching at pH 2.1 with 1 M $(NH_4)_2SO_4$, the Fe solubility of Libyan dust ~~Libya dust~~ was 7.2% (Fig. ~~S10~~S4), which was from around 3 to 7 times lower compared to that of the CFA samples (Fig. 1). At around pH 2 conditions in the presence of oxalate and high $(NH_4)_2SO_4$ concentration, the Fe solubility of Libyan dust ~~Libya dust~~ rose to ~13.6% (Fig. ~~S10~~S4), which is still 4 times lower than that of Krakow ash and around 1.5 lower than Aberthaw and Shandong ash (Fig. 2). The Fe solubilities of the Libyan dust observed in this study are comparable with those of the Tibesti dust (Tibesti Mountains, Libya, 25.583333N/16.516667E) in Ito and Shi (2016) at similar experimental conditions.

The enhanced Fe solubility in CFA compared to mineral dust could be primarily related to the different Fe speciation (Fig~~s~~. 5 ~~and S2~~). CFA contained more highly reactive Fe and magnetite but less hematite and goethite than mineral dust.

Although mineral dust is the largest contribution to aerosol Fe while CFA accounts for only a few percent, atmospheric processing of CFA may result in a larger than expected contribution of bio-accessible ~~bioavailable~~ Fe deposited to the surface ocean. It is thus important to quantify the amount and nature of CFA in atmospheric particles.

5.3 Comparison of modelled Fe solubility with field measurements

The model results obtained using ~~the emission inventory from Rathod et al. (2020) and~~ the new dissolution scheme for the proton + oxalate-promoted dissolution (Table 1) in Test 1 and Test 3 provided a better estimate of ~~dissolved Fe~~aerosol Fe solubility over the Bay of Bengal than the other tests (Figs. ~~8, 9,~~ and ~~S7~~S3). At the same time, the new model improved the agreement of aerosol Fe solubility from Test 0 (~~70~~68% ± ~~4~~5%) to Test 1 (~~44~~35% ± ~~3~~2%) and Test 3 (~~48~~47% ± 1%) with the field data (25% ± 3%) but still overestimated it after 22 January 2009, when open biomass burning sources become dominant ~~(Fig. 8)~~(Bikkina et al., 2020) as also shown in Fig. 8 and Table S4. This could be due to the unrepresentative Fe speciation used in Test 1 and Test 3 for biomass burning over the Bay of Bengal. To reduce the uncertainty in model predictions, emission inventories could be improved through a comprehensive characterization of Fe species in combustion aerosol particles.

The revised model also enabled us to predict sensitivity to a more dynamic range of pH changes, particularly between anthropogenic combustion and biomass burning by the suppression of the oxalate-promoted dissolution at pH lower than 2. In Test 0, the dissolution rate was assumed to be independent from the pH for extremely acidic solutions (pH <2). . The results show that the proton-promoted dissolution scheme in Test 2 significantly overestimated aerosol dissolved FeFe solubility (Figs. 8, 9 and S37), which indicates the suppression of the proton + oxalate-promoted dissolution at pH < 2. In Fig. 10S5, the model estimates of surface concentration of dissolved Feaerosol Fe solubility over the Bay of Bengal considerably improved in Test 1 (RMSE 11) compared to Test 0 (RMSE 21), but more work is needed to improve size-resolved Fe emission, transport, and deposition.. The model results in Test 1 also indicate a larger contribution of pyrogenic dissolved Fe over regions with strong anthropogenic combustion sources to the atmospheric Fe loading such over as East Asia (Fig. 11), but a smaller contribution of biomass burning sources downwind from tropical biomass burning regions (Fig. 1112). We demonstrated that the implementation of the new Fe dissolution scheme, including a rapid Fe release at the initial stage and highly acidic conditions, enhanced the model estimates. However, in Test 1, we turned off the photo-reductive dissolution scheme (Ito, 2015), which was based on the laboratory measurements in Chen and Grassian (2013). To determine the photoinduced dissolution kinetics of CFA particles it is necessary to account for the effect of high concentration of $(NH4)_2SO_4$ on photo-reductive dissolution rate which should be considered in future research.

Data availability statement

The new dissolution schemes for the proton-promoted and oxalate-promoted dissolution are reported in Table 1. Table S1 reports the concentrations of H_2SO_4, $H_2C_2O_4$ and $(NH_4)_2SO_4$ in the experiment solutions, the original and final pH from model estimates (including H^+ concentrations and activities), and the pH measurements for the solution with low ionic strength. Table S2 S3 contains the summary of the concentration and activity of total oxalate ions, $C_2O_4^{2-}$, and $HC_2O_4^-$ in the experiment solutions calculated using the E-AIM model III. The observations of the surface mass concentration of aerosol total Fe, dissolved Fe and Fe solubility for the fine mode ($PM_{2.5}$) over the Bay of Bengal are from Bikkina et al. (2020) and are available at https://pubs.acs.org/doi/10.1021/acsearthspacechem.0c00063. The modelled mass concentrations of total Fe in aerosol particles and the aerosol Fe solubilities over the Bay of Bengal are reported in Table S4 and Table S5, respectively. The Fe speciation, the measurements of the Fe dissolution kinetics, and the results of the IMPACT model for each sensitivity simulation (Test 0-3) can be downloaded at: https://doi.org/10.25500/edata.bham.00000702.

Author contributions

CB, ZS, and AI designed the experiments and discussed the results. ZS supervised the experimental and data analyses. CB conducted the experiments and the data analysis with contributions from ZS, AI, MDK and ND. ND, ZS and KI performed the XANES measurements. AI developed the model of the dissolution kinetics and performed the model simulations. Krakow and Aberthaw ash were provided by TJ, while Shandong ash was provided by WL. Soil 5 from Libya was collected by ND. CB prepared the article with contributions from MDK and all the other co-authors.

Competing interests

The authors declare that they have no conflict of interest.

Acknowledgments

CB is funded by the Natural Environment Research Council (NERC) CENTA studentship (grant no. NE/L002493/1). Support for this research was provided to AI by JSPS KAKENHI (grant no. 20H04329), Integrated Research Program for Advancing Climate Models (TOUGOU) (grant no. JPMXD0717935715) from the Ministry of Education, Culture, Sports, Science and Technology (MEXT), Japan. We acknowledge Diamond Light Source for time on Beamline/Lab I18 under the Proposals: SP22244-1; SP12760-1; SP10327-1.

Financial support

This research has been supported by the Natural Environment Research Council CENTA-DTP (grant no. NE/L002493/1), JSPS KAKENHI (grant no. 20H04329), the Integrated Research Program for Advancing Climate Models (TOUGOU) (grant no. JPMXD0717935715).

Table 1. Constants used to calculate Fe dissolution rates for fossil fuel combustion aerosols, based on laboratory experiments conducted at high ionic strength.

Stage	Kinetic	Scheme	Rate constant - k(pH, T)[a]	m[c]
I	Fast	Proton	$7.61 \times 10^{-6}\exp[E(pH)^{b} \times (1/298 - 1/T)]$	0.241
II	Intermediate	Proton	$1.91 \times 10^{-7}\exp[E(pH)^{b} \times (1/298 - 1/T)]$	0.195
III	Slow	Proton	$2.48 \times 10^{-7}\exp[E(pH)^{b} \times (1/298 - 1/T)]$	0.843
I	Fast	Proton + Oxalate	$5.54 \times 10^{-6}\exp[E(pH)^{b} \times (1/298 - 1/T)]$	0.209
II	Intermediate	Proton + Oxalate	$1.50 \times 10^{-7}\exp[E(pH)^{b} \times (1/298 - 1/T)]$	0.091
III	Slow	Proton + Oxalate	$1.77 \times 10^{-8}\exp[E(pH)^{b} \times (1/298 - 1/T)]$	0.204

[a] k(pH, T) is the pH and temperature dependent 'far-from-equilibrium' rate constant (moles Fe g^{-1} s^{-1}). The Fe dissolution scheme assumes 3 rate constants "fast", "intermediate" and "slow" for the proton- and oxalate-promoted dissolution. The parameters were fitted to our measurements for Krakow ash.

[b] $E(pH) = -1.56 \times 10^{3} \times pH + 1.08 \times 10^{4}$. The parameters were fitted to the measurements for soils (Bibi et al., 2014).

[c] m is the reaction order with respect to aqueous phase protons, which was determined by linear regression from our experimental data in the pH range between 2 and 3 for proton- and oxalate-promoted dissolution schemes.

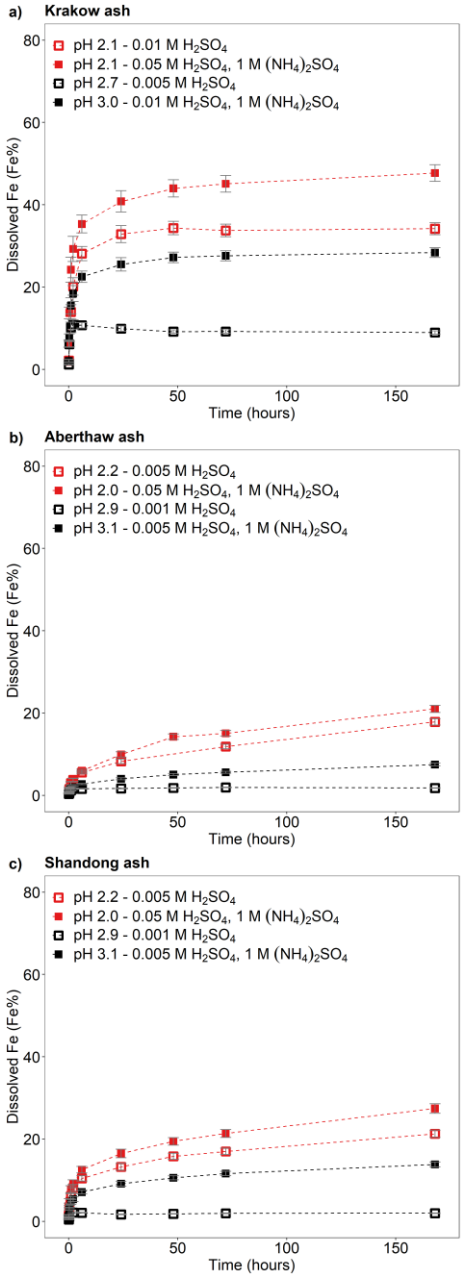

Figure 1: Fe dissolution kinetics of a) Krakow ash, b) Aberthaw ash and c) Shandong ash in H_2SO_4 solutions (open rectangles) and with 1 M $(NH_4)_2SO_4$ (filled rectangles). The molar concentrations of H_2SO_4 and $(NH_4)_2SO_4$ in the experiment solutions are shown. The final pH of the experiment solutions is also reported, which was calculated using the E-AIM model III for aqueous solution (Wexler and Clegg, 2002) accounting for the buffer capacity of the CFA samples (Experiments 1-2 in Table S1). The experiments conducted at around pH 2 are in red, while the experiments at around pH 3 are in black. The data uncertainty was estimated using the error propagation formula.

Formatted: Subscript

Formatted: Subscript

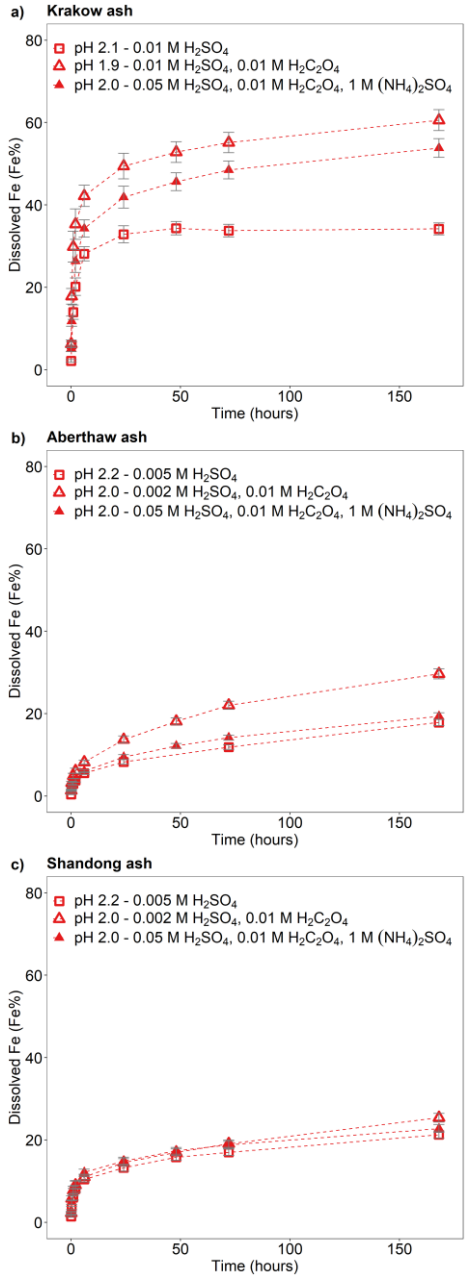

Figure 2: Fe dissolution kinetics of a) Krakow ash, b) Aberthaw ash, and c) Shandong ash in H_2SO_4 solutions at around pH 2 (red open rectangles), with 0.01 M $H_2C_2O_4$ (red open triangles), and 1 M $(NH_4)_2SO_4$ (red filled triangles). The molar concentrations of H_2SO_4, $H_2C_2O_4$ and $(NH_4)_2SO_4$ in the experiment solutions are shown. The final pH of the experiment solutions is also reported, which was calculated using the E-AIM model III for aqueous solution (Wexler and Clegg, 2002) accounting for the buffer capacity of the CFA samples (Experiments 1, 3-4 at around pH 2). The data uncertainty was estimated using the error propagation formula.

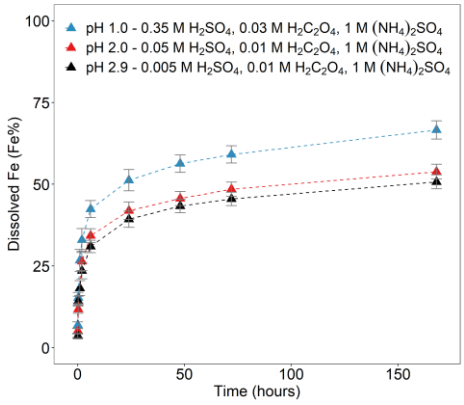

Figure 3: Fe dissolution kinetics of Krakow ash in H_2SO_4 solutions at pH 1.0 with 0.03 M $H_2C_2O_4$ and 1 M $(NH_4)_2SO_4$ (blue filled triangles), at pH 2.0 with 0.01 M $H_2C_2O_4$ and 1 M $(NH_4)_2SO_4$ (red filled triangles), and at pH 2.9 with 0.01 M $H_2C_2O_4$ and 1 M $(NH_4)_2SO_4$ (black filled triangles). The molar concentrations of H_2SO_4, $H_2C_2O_4$ and $(NH_4)_2SO_4$ in the experiment solutions are shown. The final pH of the experiment solutions is also reported, which was calculated using the E-AIM model III for aqueous solution (Wexler and Clegg, 2002) accounting for the buffer capacity of the CFA samples (Experiment 7 at pH 1.0, Experiment 3 at pH 2.0, and Experiment 3 at pH 2.9 in Table S1). The data uncertainty was estimated using the error propagation formula.

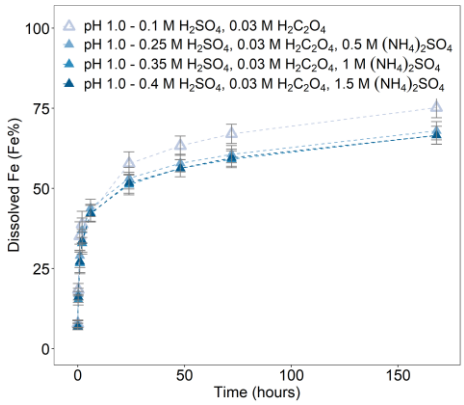

Figure 4: Fe dissolution kinetics of Krakow ash in H_2SO_4 solutions at pH 1.0 with 0.03 M $H_2C_2O_4$ and concentration of $(NH_4)_2SO_4$ from 0 to 1.5 M. The molar concentrations of H_2SO_4, $H_2C_2O_4$ and $(NH_4)_2SO_4$ in the experiment solutions are shown. The final pH of the experiment solutions is also reported, which was calculated using the E-AIM model III for aqueous solution (Wexler and Clegg, 2002) accounting for the buffer capacity of the CFA samples (Experiments 5-8 in Table S1). The data uncertainty was estimated using the error propagation formula.

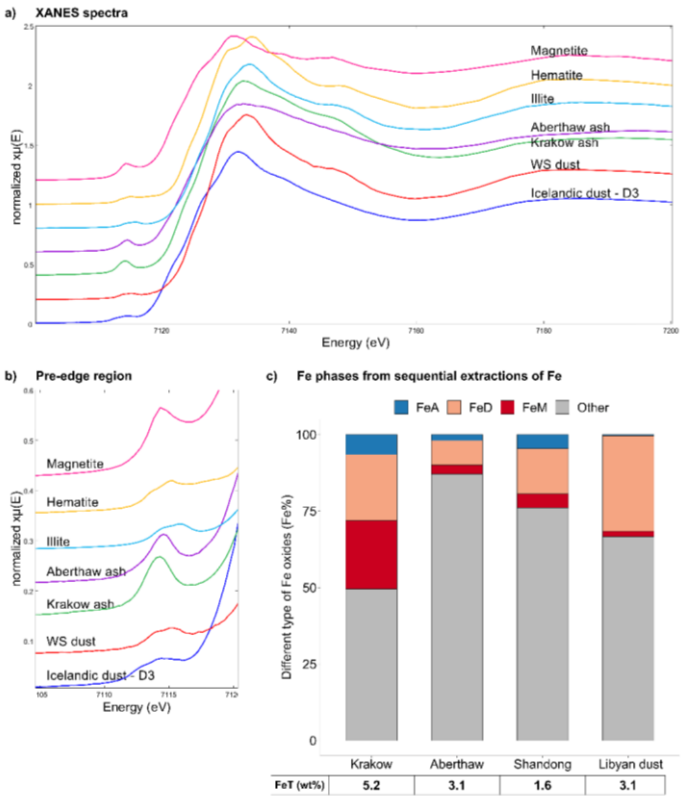

Figure 5: Fe speciation in CFA and mineral dust samples. a-b) Fe K-edge XANES spectra of Krakow ash, Aberthaw ash, magnetite, hematite, and illite standards, mineral dust from the Dyngjusandur dust hotspot in Iceland - D3 (Baldo et al., 2020), and mineral dust from western Sahara - WS dust (Shi et al., 2011b). c) Percentages of ascorbate Fe (amorphous Fe, FeA), dithionite Fe (~~FeD~~goethite/hematite, FeD), magnetite Fe (FeM), and other Fe (including Fe in aluminosilicates) to the total Fe (FeT) in the ~~coal fly ash~~CFA samples and ~~mineral dust from Africa (Libya dust)~~Libyan dust precursor. The FeT (as %wt.) ~~was~~ is given below each sample column. The data uncertainty was estimated using the error propagation formula: 4% for FeA/FeT, 11% for FeD/FeT, 12% for FeM/FeT, and 2 % for FeT.

Formatted: Centered

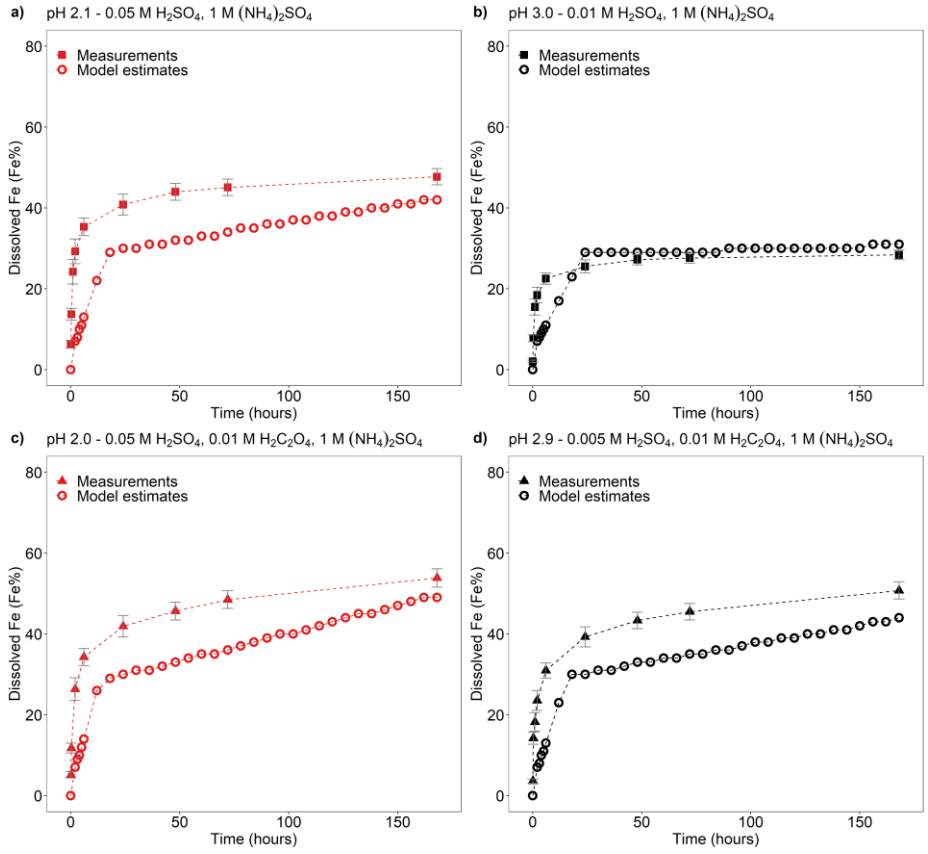

Figure 6: Comparison between the Fe dissolution kinetics of Krakow ash predicted using Eq. (1) and measured in H_2SO_4 solutions a-b) with 1 M $(NH_4)_2SO_4$, c-d) with 0.01 M $H_2C_2O_4$ and 1 M $(NH_4)_2SO_4$. The molar concentrations of H_2SO_4, $H_2C_2O_4$ and $(NH_4)_2SO_4$ in the experiment solutions are shown. The final pH of the experiment solutions is also reported, which was calculated using the E-AIM model III for aqueous solution (Wexler and Clegg, 2002) accounting for the buffer capacity of the CFA samples (Experiments 2-3 in Table S1). The experiments conducted at around pH 2 are in red, while the experiments at around pH 3 are in black. The data uncertainty was estimated using the error propagation formula.

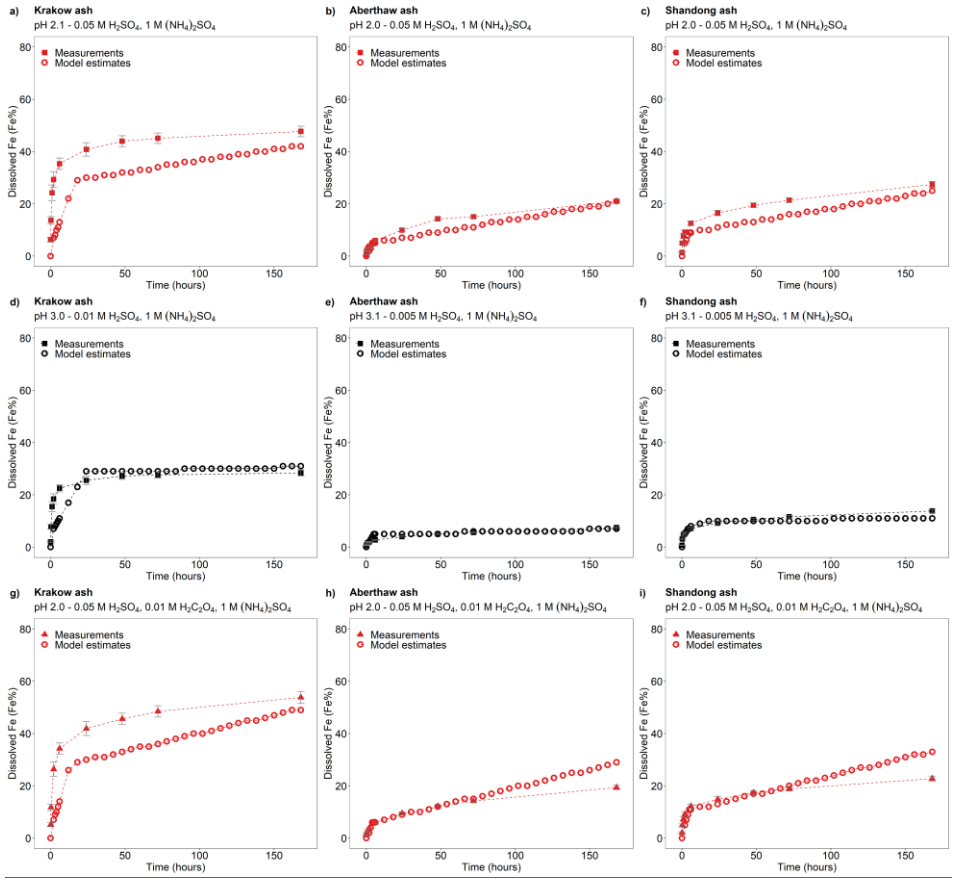

Figure 7: Comparison between the Fe dissolution kinetics of Krakow, Aberthaw, and Shandong ashes predicted using Eq. (1) and measured in a-c) H_2SO_4 solutions at around pH 2 with 1 M $(NH_4)_2SO_4$ (Experiments 2 at around pH 2 in Table S1), d-f) H_2SO_4 solutions at around pH 3 with 1 M $(NH_4)_2SO_4$ (Experiments 2 at around pH 3 in Table S1), g-i) H_2SO_4 solutions at pH 2.0 with 0.01 M $H_2C_2O_4$ and 1 M $(NH_4)_2SO_4$ (Experiments 3 at pH 2.0 in Table S1). The molar concentrations of H_2SO_4, $H_2C_2O_4$ and $(NH_4)_2SO_4$ in the experiment solutions are shown. The final pH of the experiment solutions is also reported, which was calculated using the E-AIM model III for aqueous solution (Wexler and Clegg, 2002) accounting for the buffer capacity of the CFA samples.

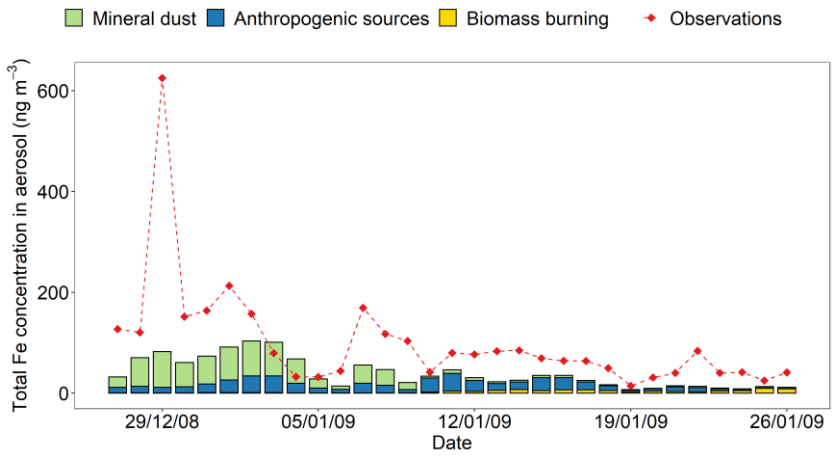

Figure 8: ~~Surface~~ Mass **concentration of** total **Fe in $PM_{2.5}$ aerosol particles over the Bay of Bengal from 27 December 2008 to 26 January 2009. Observations are from Bikkina et al. (2020) (red filled diamonds).** ~~Aerosol Fe was calculated along the cruise tracks using the IMPACT model.~~ The concentrations of total Fe were calculated along the cruise tracks in the North Bay of Bengal (27 December 2008 - 10 January 2009) and the South Bay of Bengal (11-26 January 2009) using the IMPACT model. The total Fe emissions from anthropogenic combustion sources (ANTHRO) and biomass burning (BB) were estimated using the emission inventory of **(Ito et al., 2018)**, whereas Fe emissions from mineral dust sources (DUST) were dynamically simulated **(Ito et al., 2021a)**.

~~The total Fe emission in anthropogenic aerosols was estimated using Fe emission factors by each sector such as energy, industry, and iron and steel industry for the simulation years (Ito et al., 2018) in sensitivity Test 0 (yellow filled circles), while the mineral specific emission inventory for the year 2010 by Rathod et al. (2020) was used in the other tests. The contribution of mineral dust sources, anthropogenic sources and biomass burning to total Fe is shown for Test 1-3.~~

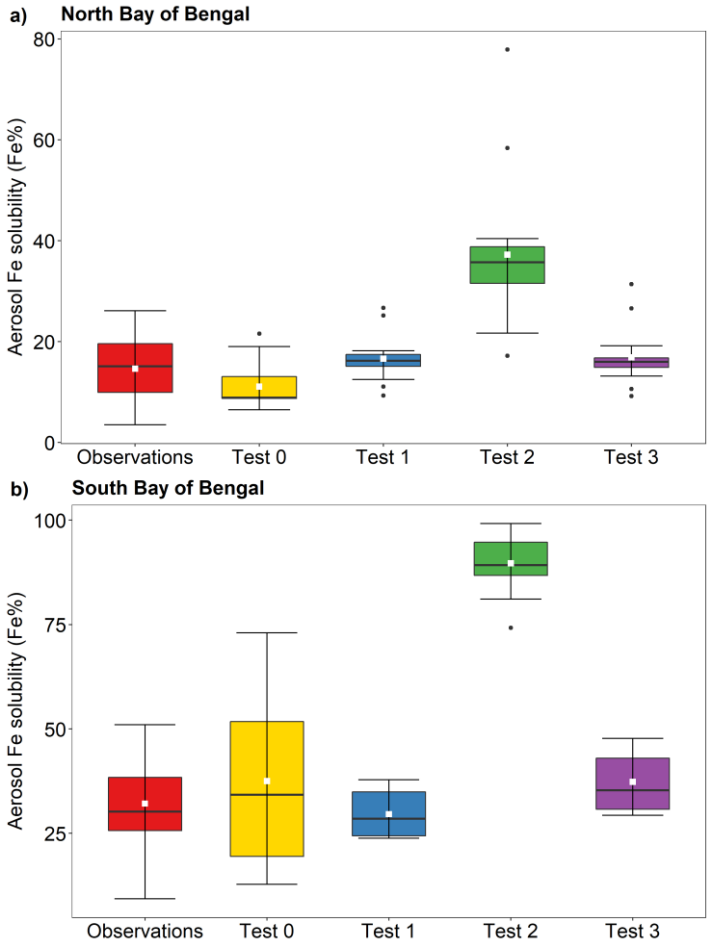

Figure 9: Fe solubility in $PM_{2.5}$ aerosol particles over a) the North Bay of Bengal, and b) the South Bay of Bengal from 27 December 2008 to 26 January 2009. Observations are from Bikkina et al. (2020). Model estimates of Test 0, Test 1, Test 2, and Test 3 were calculated along the cruise tracks using the IMPACT model. In Test 0, we run the model without upgrades **(Ito et al., 2021a)** and applying the proton-promoted, oxalate-promoted, and photoinduced dissolution schemes for combustion aerosols in Table S6 (Ito, 2015). The proton + oxalate dissolution scheme (Table 1) was applied in Test 1 and 3, while proton-promoted dissolution is used for Test 2. We adopted the base mineralogy for anthropogenic Fe emissions (Rathod et al., 2020) in Test 1 and 2. In Test 3, the Fe speciation of Krakow ash was used for all combustion sources. The small white square within the box shows the mean. The solid line within the box indicates the median. The lower and upper hinges correspond to the 25^{th} and 75^{th} percentiles. The whiskers above and below the box indicate the 1.5 × interquartile range, and the data outside this range are plotted individually.~~Surface concentration of dissolved Fe in $PM_{2.5}$ aerosol particles over the Bay of Bengal from 27 December 2008 to 26 January 2009. Observations are from Bikkina et al. (2020) (red filled diamonds). Aerosol dissolved Fe was calculated along the cruise tracks using the IMPACT model. In Test 0 (yellow filled circles), we ran the model without upgrades in the Fe dissolution scheme (Ito et al., 2021a), and applying the proton-promoted, oxalate-promoted and photoinduced dissolution schemes for combustion aerosols. The contribution of mineral dust sources, anthropogenic sources and biomass burning is shown for Test 1-3. The proton + oxalate dissolution scheme (Table 1) was applied in Test 1 and 3, while proton-promoted dissolution is used for Test 2. We adopted the mineral-specific inventory for anthropogenic Fe emissions (Rathod et al., 2020) in Test 1 and 2. In Test 3, the Fe speciation of Krakow ash was used for all combustion sources.~~

Formatted: Caption, Don't keep with next

Formatted: Superscript

Formatted: Superscript

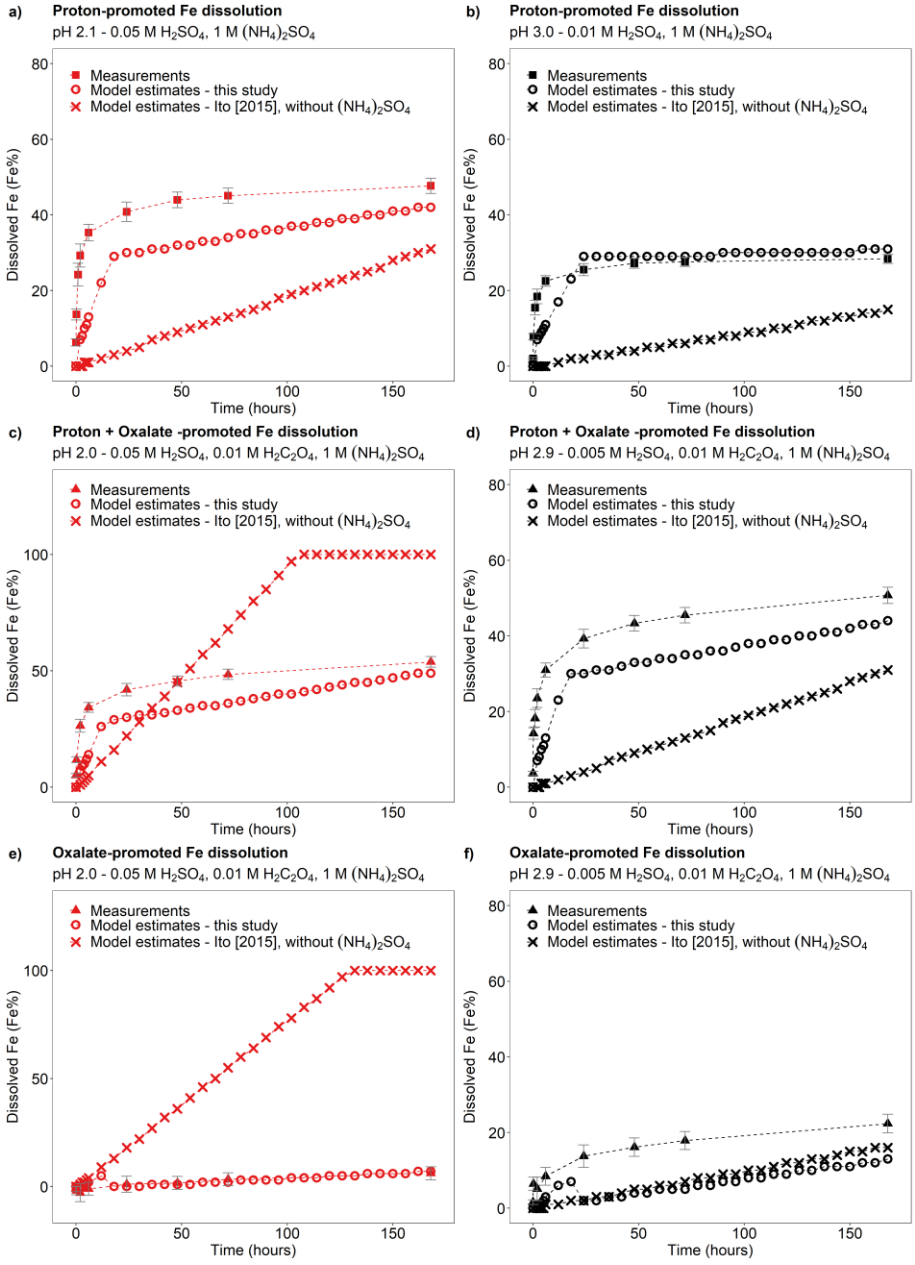

Figure 10: ~~Comparison~~ Comparison between the Fe dissolution kinetics of Krakow ash calculated using the original (Ito, 2015) and the new dissolution scheme (Tables 1 and S6). a-b) Proton-promoted Fe dissolution in H_2SO_4 solutions with 1 M $(NH_4)_2SO_4$ at pH 2.1 (a), and at pH 3.0 (b) (Experiment 2 at pH 2.1, and Experiment 2 at pH 3.0 in Table S1). c-d) Proton + oxalate promoted Fe dissolution in H_2SO_4 solutions with 0.01 M $H_2C_2O_4$ and 1 M $(NH_4)_2SO_4$ at pH 2.0 (c), and at pH 2.9 (d) (Experiment 3 at pH 2.0, and Experiment 3 at pH 2.9 in Table S1). The Fe dissolution kinetics were predicted using the rate constants in Table 1 calculated in this study (open circles) and the dissolution scheme for combustion aerosols in Ito (2015) (cross marks). Note that the dissolution scheme in Ito (2015) was calculated based on laboratory measurements conducted at low ionic strength. e-f) Contribution of the oxalate-

promoted dissolution to dissolved Fe estimated using Eq. (3). The molar concentrations of H_2SO_4, $H_2C_2O_4$ and $(NH_4)_2SO_4$ in the experiment solutions are shown. The final pH of the experiment solutions is also reported, which was calculated using the E-AIM model III for aqueous solution (Wexler and Clegg, 2002) accounting for the buffer capacity of the CFA samples

~~between observations and model estimates of Fe solubility in $PM_{2.5}$ aerosol particles over the Bay of Bengal from 27 December 2008 to 26 January 2009. Observations are from Bikkina et al. (2020). Aerosol Fe solubility was calculated along the cruise tracks using the IMPACT model. The Taylor diagram summarizes the statistics for the comparison between observations of aerosol Fe solubility and the different simulations (Test 0-3). The dashed curves in blue indicate the standard deviation values. The curves in red denote the root-mean-squared difference between the observational data and the model predictions. The dashed lines in black represent the correlation coefficients.~~

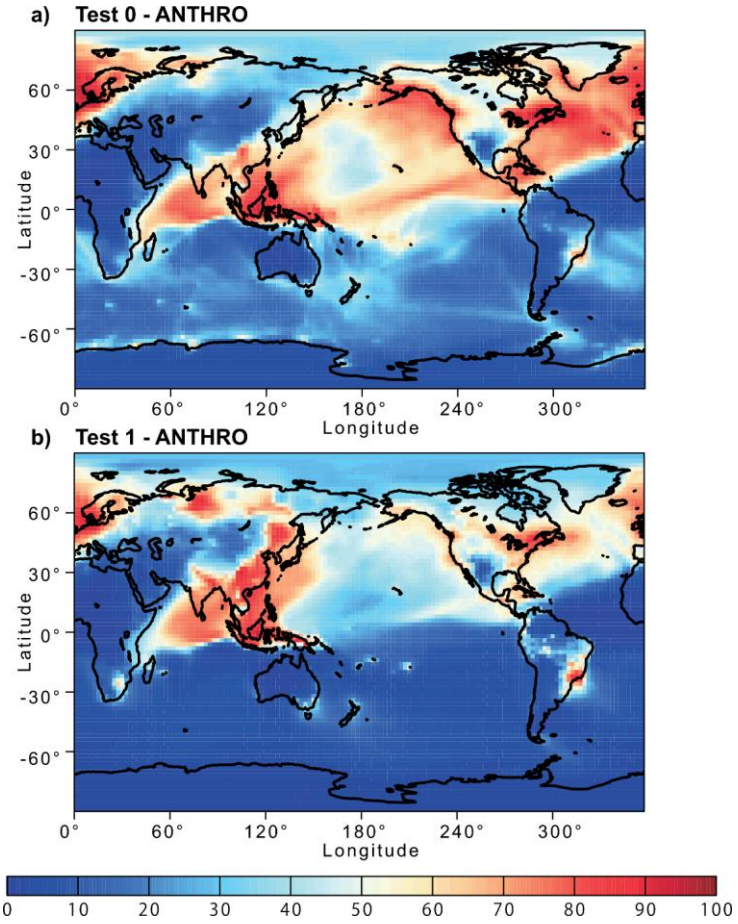

Figure 1112: Percentage contribution of anthropogenic combustion (ANTHRO) aerosol to the atmospheric dissolved Fe concentration ~~Proportion (%) of pyrogenic dissolved Fe in aerosol dissolved Fe concentration~~ near the ground surface from a) Test 0 and b) Test 1 for December 2008 and January 2009. In Test 0, we ran the model without upgrades in the Fe dissolution scheme (Ito et al., 2021a) and applying the proton-promoted, oxalate-promoted and photoinduced dissolution schemes for combustion aerosols in Table ~~S3~~ S6 (Ito, 2015). The proton + oxalate dissolution scheme (Table 1) was applied in Test 1 and we adopted the base mineralogy ~~mineral-specific inventory~~ for anthropogenic Fe emissions (Rathod et al., 2020).

Formatted: Normal

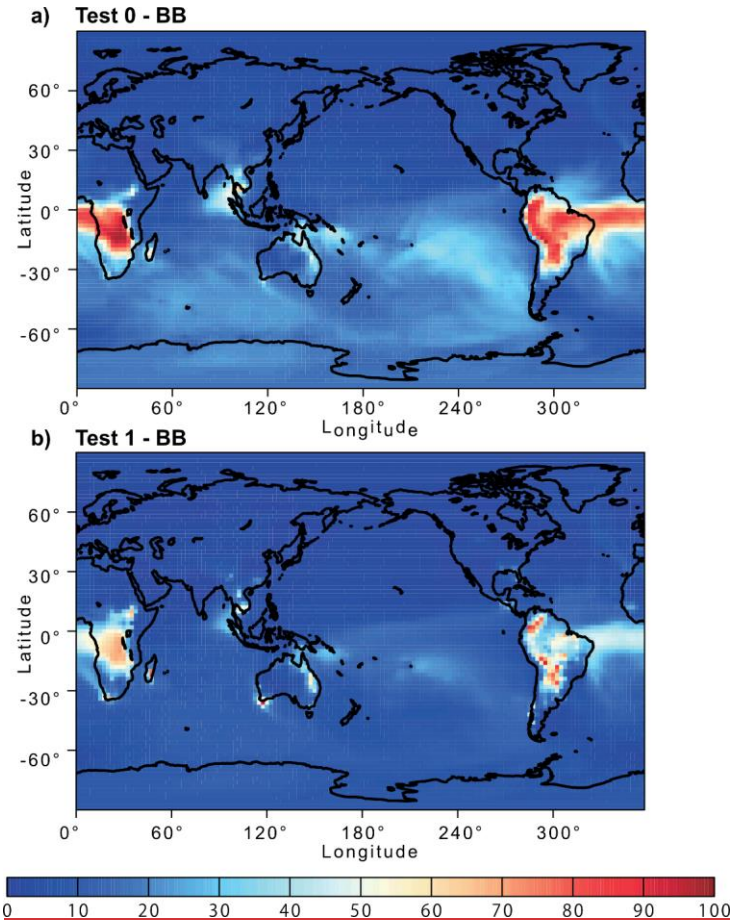

Figure 12: Percentage contribution of biomass burining (BB) aerosol to the atmospheric dissolved Fe concentration near the ground surface from a) Test 0 and b) Test 1 for December 2008 and January 2009. In Test 0, we ran the model without upgrades in the Fe dissolution scheme (Ito et al., 2021a) and applying the proton-promoted, oxalate-promoted and photoinduced dissolution schemes for combustion aerosols in Table S6 (Ito, 2015). The proton + oxalate dissolution scheme (Table 1) was applied in Test 1 and we adopted the base mineralogy for anthropogenic Fe emissions (Rathod et al., 2020).

Formatted: Keep with next

Formatted: Justified

Formatted: Centered

References

Baker, A. R., Li, M., and Chance, R.: Trace Metal Fractional Solubility in Size-Segregated Aerosols From the Tropical Eastern Atlantic Ocean, Global Biogeochem., 34, e2019GB006510, doi: 10.1029/2019GB006510, 2020.

Baker, A. R., Kanakidou, M., Nenes, A., Myriokefalitakis, S., Croot, P. L., Duce, R. A., Gao, Y., Guieu, C., Ito, A., Jickells, T. D., Mahowald, N. M., Middag, R., Perron, M. M. G., Sarin, M. M., Shelley, R., and Turner, D. R.: Changing atmospheric acidity as a modulator of nutrient deposition and ocean biogeochemistry, Sci. Adv., 7, eabd8800, doi: 10.1126/sciadv.abd8800, 2021.

Baldo, C., Formenti, P., Nowak, S., Chevaillier, S., Cazaunau, M., Pangui, E., Di Biagio, C., Doussin, J. F., Ignatyev, K., Dagsson-Waldhauserova, P., Arnalds, O., MacKenzie, A. R., and Shi, Z.: Distinct chemical and mineralogical composition of Icelandic dust compared to northern African and Asian dust, Atmos. Chem. Phys., 20, 13521-13539, doi: 10.5194/acp-20-13521-2020, 2020.

Bibi, I., Singh, B., and Silvester, E.: Dissolution kinetics of soil clays in sulfuric acid solutions: Ionic strength and temperature effects, Appl. Geochem., 51, 170-183, doi: 10.1016/j.apgeochem.2014.10.004, 2014.

Bikkina, S., Kawamura, K., Sarin, M., and Tachibana, E.: ^{13}C Probing of Ambient Photo-Fenton Reactions Involving Iron and Oxalic Acid: Implications for Oceanic Biogeochemistry, ACS Earth Space Chem., 4, 964-976, doi: 10.1021/acsearthspacechem.0c00063, 2020.

Blissett, R. S., and Rowson, N. A.: A review of the multi-component utilisation of coal fly ash, Fuel, 97, 1-23, doi: 10.1016/j.fuel.2012.03.024, 2012.

Borgatta, J., Paskavitz, A., Kim, D., and Navea, J. G.: Comparative evaluation of iron leach from different sources of fly ash under atmospherically relevant conditions, Environ. Chem., 13, 902-912, doi: 10.1071/en16046, 2016.

Boyd, P. W., Jickells, T., Law, C. S., Blain, S., Boyle, E. A., Buesseler, K. O., Coale, K. H., Cullen, J. J., de Baar, H. J. W., Follows, M., Harvey, M., Lancelot, C., Levasseur, M., Owens, N. P. J., Pollard, R., Rivkin, R. B., Sarmiento, J., Schoemann, V., Smetacek, V., Takeda, S., Tsuda, A., Turner, S., and Watson, A. J.: Mesoscale Iron Enrichment Experiments 1993-2005: Synthesis and Future Directions, Science, 315, 612-617, doi: 10.1126/science.1131669, 2007.

British Petroleum (BP): Statistical Review of World Energy 2020, available at https://www.bp.com/en/global/corporate/energy-economics/statistical-review-of-world-energy.html, (last access: 10 April 2021), 2020.

Brown, P., Jones, T., and BéruBé, K.: The internal microstructure and fibrous mineralogy of fly ash from coal-burning power stations, Environ. Pollut., 159, 3324-3333, doi: 10.1016/j.envpol.2011.08.041, 2011.

Chen, H., Laskin, A., Baltrusaitis, J., Gorski, C. A., Scherer, M. M., and Grassian, V. H.: Coal fly ash as a source of iron in atmospheric dust, Environ. Sci. Technol., 46, 2112-2120, doi: 10.1021/es204102f, 2012.

Chen, H. H., and Grassian, V. H.: Iron Dissolution of Dust Source Materials during Simulated Acidic Processing: The Effect of Sulfuric, Acetic, and Oxalic Acids, Environ. Sci. Technol., 47, 10312-10321, doi: 10.1021/es401285s, 2013.

Cornell, R. M., Posner, A. M., and Quirk, J. P.: Kinetics and mechanisms of the acid dissolution of goethite (α-FeOOH), Journal of Inorganic and Nuclear Chemistry, 38, 563-567, doi: 10.1016/0022-1902(76)80305-3, 1976.

Cornell, R. M., and Schwertmann, U.: The Iron Oxides: Structure, Properties, Reactions, Occurrence and Uses, Wiley-VCH, New York 2003.

Cwiertny, D. M., Baltrusaitis, J., Hunter, G. J., Laskin, A., Scherer, M. M., and Grassian, V. H.: Characterization and acid-mobilization study of iron-containing mineral dust source materials, J. Geophys. Res.-Atmos, 113, D05202, doi: 10.1029/2007jd009332, 2008.

Dudas, M. J., and Warren, C. J.: Submicroscopic model of fly ash particles, Geoderma, 40, 101-114, doi: 10.1016/0016-7061(87)90016-4, 1987.

Eick, M. J., Peak, J. D., and Brady, W. D.: The Effect of Oxyanions on the Oxalate-Promoted Dissolution of Goethite, SSSAJ, 63, 1133-1141, doi: doi.org/10.2136/sssaj1999.6351133x, 1999.

Emerson, E. W., Hodshire, A. L., DeBolt, H. M., Bilsback, K. R., Pierce, J. R., McMeeking, G. R., and Farmer, D. K.: Revisiting particle dry deposition and its role in radiative effect estimates, PNAS USA, 117, 26076-26082, doi: 10.1073/pnas.2014761117, 2020.

Fu, H., Cwiertny, D. M., Carmichael, G. R., Scherer, M. M., and Grassian, V. H.: Photoreductive dissolution of Fe-containing mineral dust particles in acidic media, Journal of Geophysical Research, 115, D11304, doi: 10.1029/2009jd012702, 2010.

Fu, H. B., Lin, J., Shang, G. F., Dong, W. B., Grassian, V. H., Carmichael, G. R., Li, Y., and Chen, J. M.: Solubility of Iron from Combustion Source Particles in Acidic Media Linked to Iron Speciation, Environ. Sci. Technol., 46, 11119-11127, doi: 10.1021/es302558m, 2012.

Furrer, G., and Stumm, W.: The coordination chemistry of weathering: I. Dissolution kinetics of δ-Al_2O_3 and BeO, Geochim. Cosmochim. Ac.,, 50, 1847-1860, doi: 10.1016/0016-7037(86)90243-7, 1986.

Hamer, M., Graham, R. C., Amrheim, C., and Bozhilov, K. N.: Dissolution of ripidolite (Mg, Fe-chlorite) in organic and inorganic acid solutions, SSSAJ, 67, 654-661, doi: 10.2136/sssaj2003.6540, 2003.

Ito, A., and Feng, Y.: Role of dust alkalinity in acid mobilization of iron, Atmos. Chem. Phys., 10, 9237-9250, doi: 10.5194/acp-10-9237-2010, 2010.

Ito, A.: Atmospheric Processing of Combustion Aerosols as a Source of Bioavailable Iron, Environ. Sci. Technol. Lett., 2, 70-75, doi: 10.1021/acs.estlett.5b00007, 2015.

Ito, A., and Shi, Z.: Delivery of anthropogenic bioavailable iron from mineral dust and combustion aerosols to the ocean, Atmos. Chem. Phys., 16, 85-99, doi: 10.5194/acp-16-85-2016, 2016.

Ito, A., Lin, G. X., and Penner, J. E.: Radiative forcing by light-absorbing aerosols of pyrogenetic iron oxides, Sci. Rep., 8, 7347, doi: 10.1038/s41598-018-25756-3, 2018.

Ito, A., Myriokefalitakis, S., Kanakidou, M., Mahowald, N. M., Scanza, R. A., Hamilton, D. S., Baker, A. R., Jickells, T., Sarin, M., Bikkina, S., Gao, Y., Shelley, R. U., Buck, C. S., Landing, W. M., Bowie, A. R., Perron, M. M. G., Guieu, C., Meskhidze, N., Johnson, M. S., Feng, Y., Kok, J. F., Nenes, A., and Duce, R. A.: Pyrogenic iron: The missing link to high iron solubility in aerosols, Sci. Adv., 5, eaau7671 doi: 10.1126/sciadv.aau7671, 2019.

Ito, A., Adebiyi, A. A., Huang, Y., and Kok, J. F.: Less atmospheric radiative heating by dust due to the synergy of coarser size and aspherical shape, Atmos. Chem. Phys., 21, 16869–16891, doi: 10.5194/acp-21-16869-2021, 2021a.

Ito, A., Ye, Y., Baldo, C., and Shi, Z.: Ocean fertilization by pyrogenic aerosol iron, npj Clim. Atmos. Sci., 4, 30, doi: 10.1038/s41612-021-00185-8, 2021b.

Jickells, T., and Moore, C. M.: The importance of Atmospheric Deposition for Ocean Productivity, Annu. Rev. Ecol. Evol. Syst., 46, 481-501, doi: 10.1146/annurev-ecolsys-112414-054118, 2015.

Jickells, T. D., An, Z. S., Andersen, K. K., Baker, A. R., Bergametti, G., Brooks, N., Cao, J. J., Boyd, P. W., Duce, R. A., Hunter, K. A., Kawahata, H., Kubilay, N., laRoche, J., Liss, P. S., Mahowald, N., Prospero, J. M., Ridgwell, A. J., Tegen, I., and Torres, R.: Global iron connections between desert dust, ocean biogeochemistry, and climate, Science, 308, 67-71, doi: 10.1126/science.1105959, 2005.

Johnson, M. S., and Meskhidze, N.: Atmospheric dissolved iron deposition to the global oceans: effects of oxalate-promoted Fe dissolution, photochemical redox cycling, and dust mineralogy, Geoscientific Model Development, 6, 1137-1155, doi: 10.5194/gmd-6-1137-2013, 2013.

Jones, D. R.: The Leaching of Major and Trace Elements from Coal Ash, in: Environmental Aspects of Trace Elements in Coal, edited by: Swaine, D. J., and Goodarzi, F., Springer Netherlands, Dordrecht, 221-262, 1995.

Kanakidou, M., Myriokefalitakis, S., and Tsigaridis, K.: Aerosols in atmospheric chemistry and biogeochemical cycles of nutrients, Environ. Res. Lett., 13, 063004, doi: 10.1088/1748-9326/aabcdb, 2018.

Kawamura, K., and Bikkina, S.: A review of dicarboxylic acids and related compounds in atmospheric aerosols: Molecular distributions, sources and transformation, Atmos. Res., 170, 140-160, doi: 10.1016/j.atmosres.2015.11.018, 2016.

Kim, D., Xiao, Y., Karchere-Sun, R., Richmond, E., Ricker, H. M., Leonardi, A., and Navea, J. G.: Atmospheric Processing of Anthropogenic Combustion Particles: Effects of Acid Media and Solar Flux on the Iron Mobility from Fly Ash, ACS Earth Space Chem., 4, 750-761, doi: 10.1021/acsearthspacechem.0c00057, 2020.

Kukier, U., Ishak, C. F., Sumner, M. E., and Miller, W. P.: Composition and element solubility of magnetic and non-magnetic fly ash fractions, Environ. Pollut., 123, 255-266, doi: 10.1016/S0269-7491(02)00376-7, 2003.

Kumar, A., Sarin, M. M., and Srinivas, B.: Aerosol iron solubility over Bay of Bengal: Role of anthropogenic sources and chemical processing, Mar. Chem., 121, 167-175, doi: 10.1016/j.marchem.2010.04.005, 2010.

Kutchko, B. G., and Kim, A. G.: Fly ash characterization by SEM–EDS, Fuel, 85, 2537-2544, doi: 10.1016/j.fuel.2006.05.016, 2006.

Lawson, M. J., Prytherch, Z. C., Jones, T. P., Adams, R. A., and BéruBé, K. A.: Iron-Rich Magnetic Coal Fly Ash Particles Induce Apoptosis in Human Bronchial Cells, Appl. Sci., 10, 8368, doi: 10.3390/app10238368, 2020.

Lee, S. O., Tran, T., Jung, B. H., Kim, S. J., and Kim, M. J.: Dissolution of iron oxide using oxalic acid, Hydrometallurgy, 87, 91-99, doi: 10.1016/j.hydromet.2007.02.005, 2007.

Li, J., Anderson, J. R., and Buseck, P. R.: TEM study of aerosol particles from clean and polluted marine boundary layers over the North Atlantic, J. Geophys. Res.-Atmos, 108, doi: 10.1029/2002JD002106, 2003.

Li, W. J., Xu, L., Liu, X. H., Zhang, J. C., Lin, Y. T., Yao, X. H., Gao, H. W., Zhang, D. Z., Chen, J. M., Wang, W. X., Harrison, R. M., Zhang, X. Y., Shao, L. Y., Fu, P. Q., Nenes, A., and Shi, Z. B.: Air pollution-aerosol interactions produce more bioavailable iron for ocean ecosystems, Sci. Adv., 3, e1601749, doi: 10.1126/sciadv.1601749, 2017.

Mahowald, N. M., Kloster, S., Engelstaedter, S., Moore, J. K., Mukhopadhyay, S., McConnell, J. R., Albani, S., Doney, S. C., Bhattacharya, A., Curran, M. A. J., Flanner, M. G., Hoffman, F. M., Lawrence, D. M., Lindsay, K., Mayewski, P. A., Neff, J., Rothenberg, D., Thomas, E., Thornton, P. E., and Zender, C. S.: Observed 20th century desert dust variability: impact on climate and biogeochemistry, Atmos. Chem. Phys., 10, 10875-10893, doi: 10.5194/acp-10-10875-2010, 2010.

Marcotte, A. R., Anbar, A. D., Majestic, B. J., and Herckes, P.: Mineral Dust and Iron Solubility: Effects of Composition, Particle Size, and Surface Area, Atmosphere, 11, 533, doi: 10.3390/atmos11050533, 2020.

Martin, J. H.: Glacial-interglacial CO_2 change: The Iron Hypothesis, Paleoceanography, 5, 1-13, doi: 10.1029/PA005i001p00001, 1990.

Matsuo, M., Kobayashi, T., Singh, T. B., Tsurumi, M., and Ichikuni, M.: ^{57}Fe Mössbauer spectroscopic study of Japanese cedar bark — The variation in chemical states of iron due to influence of human activities, Hyperfine Interact., 71, 1255-1258, doi: 10.1007/BF02397311, 1992.

Meskhidze, N., Chameides, W. L., Nenes, A., and Chen, G.: Iron mobilization in mineral dust: Can anthropogenic SO_2 emissions affect ocean productivity?, Geophys. Res. Lett., 30, 2085, doi: 10.1029/2003gl018035, 2003.

Mills, M. M., Ridame, C., Davey, M., La Roche, J., and Geider, R. J.: Iron and phosphorus co-limit nitrogen fixation in the eastern tropical North Atlantic, Nature, 429, 292-294, doi: 10.1038/nature02550, 2004.

Moore, C. M., Mills, M. M., Milne, A., Langlois, R., Achterberg, E. P., Lochte, K., Geider, R. J., and La Roche, J.: Iron limits primary productivity during spring bloom development in the central North Atlantic, Glob. Change Biol., 12, 626-634, doi: 10.1111/j.1365-2486.2006.01122.x, 2006.

Munawer, M. E.: Human health and environmental impacts of coal combustion and post-combustion wastes, J. Sustain. Min., 17, 87-96, doi: 10.1016/j.jsm.2017.12.007, 2018.

Paris, R., Desboeufs, K. V., and Journet, E.: Variability of dust iron solubility in atmospheric waters: Investigation of the role of oxalate organic complexation, Atmos. Environ., 45, 6510-6517, doi: 10.1016/j.atmosenv.2011.08.068, 2011.

Paris, R., and Desboeufs, K. V.: Effect of atmospheric organic complexation on iron-bearing dust solubility, Atmos. Chem. Phys., 13, 4895-4905, doi: 10.5194/acp-13-4895-2013, 2013.

Poulton, S. W., and Canfield, D. E.: Development of a sequential extraction procedure for iron: implications for iron partitioning in continentally derived particulates, Chem. Geol., 214, 209-221, doi: 10.1016/j.chemgeo.2004.09.003, 2005.

Pye, H. O. T., Nenes, A., Alexander, B., Ault, A. P., Barth, M. C., Clegg, S. L., Collett Jr, J. L., Fahey, K. M., Hennigan, C. J., Herrmann, H., Kanakidou, M., Kelly, J. T., Ku, I. T., McNeill, V. F., Riemer, N., Schaefer, T., Shi, G., Tilgner, A., Walker, J. T., Wang, T., Weber, R., Xing, J., Zaveri, R. A., and Zuend, A.: The acidity of atmospheric particles and clouds, Atmos. Chem. Phys., 20, 4809-4888, doi: 10.5194/acp-20-4809-2020, 2020.

Raiswell, R., Benning, L. G., Tranter, M., and Tulaczyk, S.: Bioavailable iron in the Southern Ocean: the significance of the iceberg conveyor belt, Geochemical Transactions, 9, doi: 10.1186/1467-4866-9-7, 2008.

Rathod, S. D., Hamilton, D. S., Mahowald, N. M., Klimont, Z., Corbett, J. J., and Bond, T. C.: A Mineralogy - Based Anthropogenic Combustion - Iron Emission Inventory, J. Geophys. Res.-Atmos, 125, e2019JD032114, doi: 10.1029/2019jd032114, 2020.

Ravel, B., and Newville, M.: ATHENA, ARTEMIS, HEPHAESTUS: data analysis for X-ray absorption spectroscopy using IFEFFIT, J. Synchrotron Radiat., 12, 537-541, doi: 10.1107/S0909049505012719, 2005.

Rubasinghege, G., Lentz, R. W., Scherer, M. M., and Grassian, V. H.: Simulated atmospheric processing of iron oxyhydroxide minerals at low pH: roles of particle size and acid anion in iron dissolution, PNAS USA, 107, 6628-6633, doi: 10.1073/pnas.0910809107, 2010.

Rubin, M., Berman-Frank, I., and Shaked, Y.: Dust- and mineral-iron utilization by the marine dinitrogen-fixer Trichodesmium, Nat. Geosci., 4, 529-534, doi: 10.1038/ngeo1181, 2011.

Schlosser, C., Schmidt, K., Aquilina, A., Homoky, W. B., Castrillejo, M., Mills, R. A., Patey, M. D., Fielding, S., Atkinson, A., and Achterberg, E. P.: Mechanisms of dissolved and labile particulate iron supply to shelf waters and phytoplankton blooms off South Georgia, Southern Ocean, Biogeosciences, 15, 4973-4993, doi: 10.5194/bg-15-4973-2018, 2018.

Schwertmann, U.: Solubility and dissolution of iron oxides, Plant Soil, 130, 1-25, doi: 10.1007/BF00011851, 1991.

Seinfeld, J. H., and Pandis, S. N.: Atmospheric chemistry and physics: from air pollution to climate change, John Wiley & Sons, 2016.

Shelley, R. U., Landing, W. M., Ussher, S. J., Planquette, H., and Sarthou, G.: Regional trends in the fractional solubility of Fe and other metals from North Atlantic aerosols (GEOTRACES cruises GA01 and GA03) following a two-stage leach, Biogeosciences, 15, 2271-2288, doi: 10.5194/bg-15-2271-2018, 2018.

Shi, Z., Krom, M. D., Bonneville, S., Baker, A. R., Jickells, T. D., and Benning, L. G.: Formation of iron nanoparticles and increase in iron reactivity in the mineral dust during simulated cloud processing, Environ. Sci. Technol., 43, 6592-6596, doi: 10.1021/es901294g, 2009.

Shi, Z., Bonneville, S., Krom, M. D., Carslaw, K. S., Jickells, T. D., Baker, A. R., and Benning, L. G.: Iron dissolution kinetics of mineral dust at low pH during simulated atmospheric processing, Atmos. Chem. Phys., 11, 995-1007, doi: 10.5194/acp-11-995-2011, 2011a.

Shi, Z., Krom, M. D., Bonneville, S., Baker, A. R., Bristow, C., Drake, N., Mann, G., Carslaw, K., McQuaid, J. B., Jickells, T., and Benning, L. G.: Influence of chemical weathering and aging of iron oxides on the potential iron solubility of Saharan dust during simulated atmospheric processing, Global Biogeochem., 25, GB2010, doi: 10.1029/2010gb003837, 2011b.

Shi, Z., Krom, M. D., Jickells, T. D., Bonneville, S., Carslaw, K. S., Mihalopoulos, N., Baker, A. R., and Benning, L. G.: Impacts on iron solubility in the mineral dust by processes in the source region and the atmosphere: A review, Aeolian Res., 5, 21-42, doi: 10.1016/j.aeolia.2012.03.001, 2012.

Shi, Z., Krom, M. D., Bonneville, S., and Benning, L. G.: Atmospheric processing outside clouds increases soluble iron in mineral dust, Environ. Sci. Technol., 49, 1472-1477, doi: 10.1021/es504623x, 2015.

Shi, Z. B., Woodhouse, M. T., Carslaw, K. S., Krom, M. D., Mann, G. W., Baker, A. R., Savov, I., Fones, G. R., Brooks, B., Drake, N., Jickells, T. D., and Benning, L. G.: Minor effect of physical size sorting on iron solubility of transported mineral dust, Atmos. Chem. Phys., 11, 8459-8469, doi: 10.5194/acp-11-8459-2011, 2011c.

Sholkovitz, E. R., Sedwick, P. N., and Church, T. M.: Influence of anthropogenic combustion emissions on the deposition of soluble aerosol iron to the ocean: Empirical estimates for island sites in the North Atlantic, Geochim. Cosmochim. Ac.,, 73, 3981-4003, doi: 10.1016/j.gca.2009.04.029, 2009.

Sholkovitz, E. R., Sedwick, P. N., Church, T. M., Baker, A. R., and Powell, C. F.: Fractional solubility of aerosol iron: Synthesis of a global-scale data set, Geochim. Cosmochim. Ac.,, 89, 173-189, doi: 10.1016/j.gca.2012.04.022, 2012.

Sidhu, P. S., Gilkes, R. J., Cornell, R. M., Posner, A. M., and Quirk, J. P.: Dissolution of Iron Oxides and Oxyhydroxides in Hydrochloric and Perchloric Acids, Clays Clay Miner., 29, 269-276, doi: 10.1346/CCMN.1981.0290404, 1981.

925 Spokes, L. J., and Jickells, T. D.: Factors controlling the solubility of aerosol trace metals in the atmosphere and on mixing
926 into seawater, Aquat. Geochem., 1, 355-374, doi: 10.1007/BF00702739, 1995.

927 Srinivas, B., Sarin, M. M., and Kumar, A.: Impact of anthropogenic sources on aerosol iron solubility over the Bay of Bengal
928 and the Arabian Sea, Biogeochemistry, 110, 257-268, doi: 10.1007/s10533-011-9680-1, 2012.

929 Srinivas, B., and Sarin, M. M.: Atmospheric dry-deposition of mineral dust and anthropogenic trace metals to the Bay of
930 Bengal, J. Mar. Syst., 126, 56-68, doi: 10.1016/j.jmarsys.2012.11.004, 2013.

931 Surana, V., and Warren, I.: The leaching of goethite, Transactions of the Institute of Mining and Metallurgy, 80, C152-155,
932 1969.

933 Sutto, T. E.: Magnetite fine particle and nanoparticle environmental contamination from industrial uses of coal, Environ. Pollut.,
934 243, 528-533, doi: 10.1016/j.envpol.2018.08.080, 2018.

935 Valeev, D., Mikhailova, A., and Atmadzhidi, A.: Kinetics of Iron Extraction from Coal Fly Ash by Hydrochloric Acid
936 Leaching, Metals, 8, 533, doi: 10.3390/met8070533, 2018.

937 Valeev, D., Kunilova, I., Alpatov, A., Varnavskaya, A., and Ju, D.: Magnetite and Carbon Extraction from Coal Fly Ash Using
938 Magnetic Separation and Flotation Methods, Minerals, 9, 320, doi: 10.3390/min9050320, 2019.

939 Viollier, E., Inglett, P. W., Hunter, K., Roychoudhury, A. N., and Van Cappellen, P.: The ferrozine method revisited:
940 Fe(II)/Fe(III) determination in natural waters, Appl. Geochem., 15, 785-790, doi: 10.1016/s0883-2927(99)00097-9, 2000.

941 Waanders, F. B., Vinken, E., Mans, A., and Mulaba-Bafubiandi, A. F.: Iron Minerals in Coal, Weathered Coal and Coal Ash
942 – SEM and Mössbauer Results, Hyperfine Interact., 148, 21-29, doi: 10.1023/B:HYPE.0000003760.89706.f6, 2003.

943 Wang, R., Balkanski, Y., Boucher, O., Bopp, L., Chappell, A., Ciais, P., Hauglustaine, D., Penuelas, J., and Tao, S.: Sources,
944 transport and deposition of iron in the global atmosphere, Atmos. Chem. Phys., 15, 6247-6270, doi: 10.5194/acp-15-6247-
945 2015, 2015.

946 Wang, X. S.: Mineralogical and chemical composition of magnetic fly ash fraction, Environ. Earth Sci., 71, 1673-1681, doi:
947 10.1007/s12665-013-2571-0, 2014.

948 Warren, C. J., and Dudas, M. J.: Leachability and partitioning of elements in ferromagnetic fly ash particles, Sci. Total Environ.,
949 84, 223-236, doi: 10.1016/0048-9697(89)90385-9, 1989.

950 Wexler, A. S., and Clegg, S. L.: Atmospheric aerosol models for systems including the ions H^+, NH_4^+, Na^+, SO_4^{2-}, NO_3^-, Cl^-,
951 Br^-, and H_2O, J. Geophys. Res.-Atmos, 107, 4207, doi: 10.1029/2001JD000451, 2002.

952 Xu, N., and Gao, Y.: Characterization of hematite dissolution affected by oxalate coating, kinetics and pH, Appl. Geochem.,
953 23, 783-793, doi: 10.1016/j.apgeochem.2007.12.026, 2008.

954 Yao, Z. T., Ji, X. S., Sarker, P. K., Tang, J. H., Ge, L. Q., Xia, M. S., and Xi, Y. Q.: A comprehensive review on the applications
955 of coal fly ash, Earth-Sci. Rev., 141, 105-121, doi: 10.1016/j.earscirev.2014.11.016, 2015.

956 Yu, J. Z., Huang, X.-F., Xu, J., and Hu, M.: When Aerosol Sulfate Goes Up, So Does Oxalate: Implication for the Formation
957 Mechanisms of Oxalate, Environ. Sci. Technol., 39, 128-133, doi: 10.1021/es049559f, 2005.

958 Zhang, D., Iwasaka, Y., Shi, G., Zang, J., Matsuki, A., and Trochkine, D.: Mixture state and size of Asian dust particles
959 collected at southwestern Japan in spring 2000, J. Geophys. Res.-Atmos, 108, 4760, doi: 10.1029/2003JD003869, 2003.

960 Zhao, Y., Zhang, J., Sun, J., Bai, X., and Zheng, C.: Mineralogy, Chemical Composition, and Microstructure of Ferrospheres
961 in Fly Ashes from Coal Combustion, Energy Fuels, 20, 1490-1497, doi: 10.1021/ef060008f, 2006.

962 Zhu, X. R., Prospero, J. M., Millero, F. J., Savoie, D. L., and Brass, G. W.: The solubility of ferric ion in marine mineral
963 aerosol solutions at ambient relative humidities Mar. Chem., 38, 91-107, doi: 10.1016/0304-4203(92)90069-m, 1992.

964